Acta Materialia 210 (2021) 116829

Contents lists available at ScienceDirect

Acta Materialia

journal homepage: www.elsevier.com/locate/actamat

Ordering effects on deformation substructures and strain hardening behavior of a CrCoNi based medium entropy alloy ☆

Jiashi Miao [a,b,*], Connor Slone [a,b], Sriswaroop Dasari [c], Maryam Ghazisaeidi [b], Rajarshi Banerjee [c], Easo P. George [d,e], Michael J. Mills [a,b,*]

[a] Center for Electron Microscopy and Analysis, The Ohio State University, Columbus, OH, 43212, USA
[b] Department of Materials Science and Engineering, The Ohio State University, Columbus, OH, 43210, USA
[c] Department of Materials Science and Engineering, University of North Texas, Denton, TX 76201, USA
[d] Materials Science and Technology Division, Oak Ridge National Laboratory, Oak Ridge, TN 37831, USA
[e] Materials Science and Engineering Department, University of Tennessee, Knoxville, TN 37996, USA

ARTICLE INFO

Article history:
Received 28 October 2020
Revised 9 February 2021
Accepted 21 March 2021
Available online 25 March 2021

Keywords:
Ordering
Planar dislocation slip
Paired dislocations
Multipoles
Medium entropy alloy

ABSTRACT

A CrCoNi based medium entropy alloy with small additions of Ti, Al and Nb (denoted as $(CrCoNi)_{93}Al_4Ti_2Nb$) in the as-quenched condition, exhibits tensile properties comparable to those of the equiatomic CrCoNi alloy at room temperature. Dark field transmission electron microscopy (TEM), atomic resolution high-angle annular dark-field scanning transmission electron microscopy (HAADF-STEM) together with atom probe tomography (APT) show that spatially-localized long range ordering (LRO) $L1_2$ domains exist in this alloy. The evolution of deformation substructure with plastic deformation in this alloy was characterized using electron backscatter diffraction (EBSD), electron channeling contrast imaging (ECCI) and STEM based techniques including the recently developed weak beam dark field STEM imaging. Plastic deformation occurs by the slip of a/2<110>dislocations, which are narrowly dissociated into Shockley partial dislocations on {111} slip planes. Their dissociation distances in the $(CrCoNi)_{93}Al_4Ti_2Nb$ alloy are much smaller than the widths of the corresponding partials in the equiatomic CrCoNi alloy due to one or more of the minor alloying elements (Al, Ti, Nb). Dislocation slip in this alloy has a pronounced planar character. The leading dislocations in slip bands glide as pairs due to the existence of LRO domains. Multipoles were formed through the slip of dislocations with opposite signs on adjacent {111} slip planes. Those multipoles serve as building blocks for the formation of subgrain structures consisting of fine slip bands. The distances between slip bands were continuously refined during plastic deformation and dynamic refinement of slip bands plays a crucial role in strain hardening. The effects of LRO domains on planar dislocation slip, the deactivation of deformation twinning and strain hardening of this alloy are discussed.

1. Introduction

High entropy alloys (HEAs) or multi-principal element alloys (MPAs) have received increasing research interest for opening up a new pathway to alloy design [1–6]. Among the different types of HEAs available, the face-centered cubic (FCC) equiatomic CrMnFeCoNi alloy has been subjected to extensive study due to its excellent combination of strength, ductility and fracture toughness especially at cryogenic temperature [1,7,8].Twinning plays a critical role in the deformation of the CrMnFeCoNi alloy [8,9]. Recent studies show that the equiatomic CrCoNi medium entropy alloy has better work hardening capability, strength and ductility as compared with CrMnFeCoNi alloy or its other quaternary or ternary variants, especially at cryogenic temperature [10,11]. A reason for its superior properties is that twinning occurs earlier during the plastic deformation of CrCoNi [12]. Plastic deformation-induced FCC-to-HCP transformation was revealed as an additional reason for the improved mechanical properties of CrCoNi with the help of detailed deformation substructure characterization using advanced scanning transmission electron microscopy (STEM) [13].

* Corresponding authors.
E-mail addresses: miao.152@osu.edu (J. Miao), mills.108@osu.edu (M.J. Mills).

https://doi.org/10.1016/j.actamat.2021.116829
1359-6454/

Deformation-induced FCC-HCP transformation has been widely used in designing high entropy alloys with a superior combination of strength and ductility [14–16].

Previous studies showed that, in FCC Fe-Mn based steels, deformation mechanisms can change from dislocation-mediated plasticity to twinning-induced plasticity (TWIP), to phase transformation-induced plasticity (TRIP) with decreasing stacking fault energies (SFE) [17–21]. The SFE of CrMnFeCoNi alloy was experimentally measured to be ~30 mJ/m^2 [22], which is higher than that of the CrCoNi alloy (~18 mJ/m^2 [23] and~22 mJ/m^2 [12]). Density functional theory (DFT) calculation shows that CrCoNi alloy has a negative stacking fault energy at 0 K and thus the transition from FCC to HCP is energetically favorable, especially at cryogenic temperature [24]. Deformation twinning in CrCoNi alloy occurs through the slip of Shockley partial dislocations on adjacent {111} slip planes, while the strain induced transformation from FCC phase to HCP phase is realized through the slip of Shockley partial dislocations on every other {111} slip plane [13]. Lower stacking fault energy favors dislocation dissociation, thus facilitating both deformation twinning and FCC-to-HCP transformation. DFT calculations show that stacking fault energy in CrMnFeCoNi [25] and CrCoNi [26] fluctuate locally (that is, it varies from point to point), which may affect solid solution strengthening and dislocation slip behavior [27].

Dislocation slip may display either wavy or planar slip character. In FCC metals, there are three main factors – stacking fault energy, friction stress, and short-range ordering – that can affect the slip character [28–30]. Low stacking fault energy promotes dislocation dissociation and thus reduces the possibility of the cross slip of screw dislocations, leading to planar dislocation slip. In alloys with high friction stress, collective dislocation slip can help to overcome high friction stress and thus planar slip is energetically favored [31]. Planar dislocation slip was also observed in alloys with high stacking fault energy but exhibiting short range order [28,30]. The planarity of dislocation slip in those alloys was attributed to glide plane softening [28]. Short range order or local chemical order has been reported in CrCoNi alloy [26,32–34]. However, so far, few studies have been devoted to understanding the effects of ordering, especially long range ordering (LRO), on dislocation slip character and work hardening behavior in high entropy alloys and medium entropy alloys.

The mechanical performance of the CrCoNi medium entropy alloy can be further tailored through micro-alloying [35–40] or novel thermomechanical processing to generate heterogonous microstructures [41–45]. The minor addition of Ti and Al in CrCoNi based medium entropy [35,46,47] and CoCrFeNi based high entropy alloy [48–50] will lead to the formation of ordered $L1_2$ precipitation microstructure after aging treatment. Such MEAs and HEAs strengthened by ordered $L1_2$ precipitate have great potential for structural application due to their excellent combination of strengthen and ductility [51,52].A recent study shows that CrCoNi based medium entropy alloy with minor additions of Ti, Al and Nb has a good combination of strength, ductility and strain hardening capability after solution treatment followed by water quenching, comparable to those of the equiatomic CrCoNi alloy [53], While the aging response of the former alloy, with its potential to form $L1_2$-γ' precipitates, is of interest, that is not the central subject of the present study. Rather, this paper will focus on the detailed dislocation features and their development when Ti, Al, and Nb are in the "quenched" condition, to allow direct comparison with previous studies of the equiatomic CrCoNi alloy [13]. Previous work has indicated the absence of deformation twinning for $(CrCoNi)_{93}Al_4Ti_2Nb$ alloy in the quenched condition [53]; however, the underlying deformation substructure and its effects on work hardening behavior remain unclear and require more detailed analysis. In this work, the evolution of deformation substructure with plastic deformation was examined using electron backscatter diffraction (EBSD), electron channeling contrast imaging (ECCI) and advanced scanning transmission electron microscopy based techniques, including a recently developed weak beam dark field STEM method [54]. The correlation between deformation substructures and strain hardening behavior is analyzed in light of the role of LRO $L1_2$ domains observed in this alloy.

2. Material and experimental methods

The alloy with a nominal composition of 30.9Ni-30.5Cr-31.3Co-4.1Al-2.3Ti-0.9Nb (at.%) (denoted as $(CrCoNi)_{93}Al_4Ti_2Nb$ in this paper) was fabricated using vacuum arc melting, homogenization, quenching and cold rolling. After cold rolling, the material was further solution treated at 1050°C (the alloy's predicted solvus temperature is 1010°C) followed by water quenching (the cooling rate involved in quenching is estimated to be around several hundred degrees Celsius per second).The formation of $L1_2$ γ'-$Ni_3(Al,Ti)$ precipitates is expected to be suppressed by this quenching process [53]. To study the evolution of deformation substructure with increasing plastic deformation, tensile tests were interrupted at 0.6, 3 and 12% engineering strain. Details regarding material preparation and mechanical testing can be found elsewhere [53].

Samples for scanning electron microscopy (SEM) based characterization, including electron backscatter diffraction (EBSD) and electron channeling contrast imaging (ECCI), were mechanically ground and polished followed by a final step of mechanical polishing using 0.05 μm colloidal silica. SEM characterization was carried out in a Thermo Scientific™ Apreo SEM equipped with an EDAX Hikari OIM system. Lift-out TEM foils were prepared using a FEI Helios Nanolab™ dual beam system. Conventional transmission electron microscopy (TEM) and scanning transmission electron microscopy (STEM) imaging including weak beam dark field STEM imaging were conducted in a FEI Tecnai TF20 TEM/STEM microscope operating at an acceleration voltage of 200 kV. Details about the experimental method of weak beam dark field STEM imaging of dislocations can be found in the previous publication [54]. High resolution HAADF-STEM imaging was conducted using an aberration corrected Thermo Scientific™ Themis Z microscope operating at an acceleration voltage of 300 kV. Samples for atom probe tomography (APT) study were prepared using focused ion beam machining in a FEI Nova Nanolab 200 system. APT experiments were conducted using a CAMECA LEAP-5000XS system in the laser evaporation mode with laser pulse energy of 50 nJ. Specimens were maintained at a constant temperature of 30 K during data collection. A pulse rate of 200 KHz and detection rate 0.005-0.01 ion/pulse were used for collecting data. CAMECA IVAS 3.8.4 software was used in 3D APT data analyses and visualization. Cluster analysis was performed on the APT datasets based on the evidence of clustering/ordering from frequency distribution analysis carried out in a volume of 30 × 30 × 40 nm^3. Maximum separation method [55,56] was used to perform cluster analysis.

3. Results

3.1. Initial microstructure

Fig. 1a is an EBSD inverse pole figure (IPF) map showing the microstructure of $(CrCoNi)_{93}Al_4Ti_2Nb$ after solution treatment at 1050°C followed by water quenching, revealing a fully recrystallized microstructure. The microstructure consists of a high fraction of Σ3 twin boundaries with a length fraction of 0.47 (defined here as the total length of Σ3 boundaries divided by the total length of all boundaries including general high-angle grain boundaries). The average grain size was determined using EBSD results. Excluding twin boundaries, the average grain size of the alloy is 26 μm. When

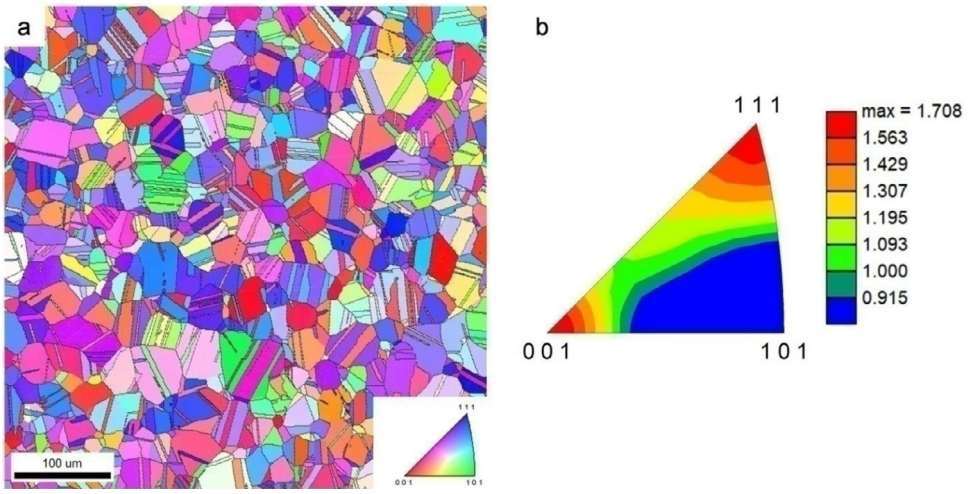

Fig. 1. EBSD characterization of the microstructure of $(CrCoNi)_{93}Al_4Ti_2Nb$ alloy: (a) inverse pole figure map; and (b) texture inverse pole figure map.

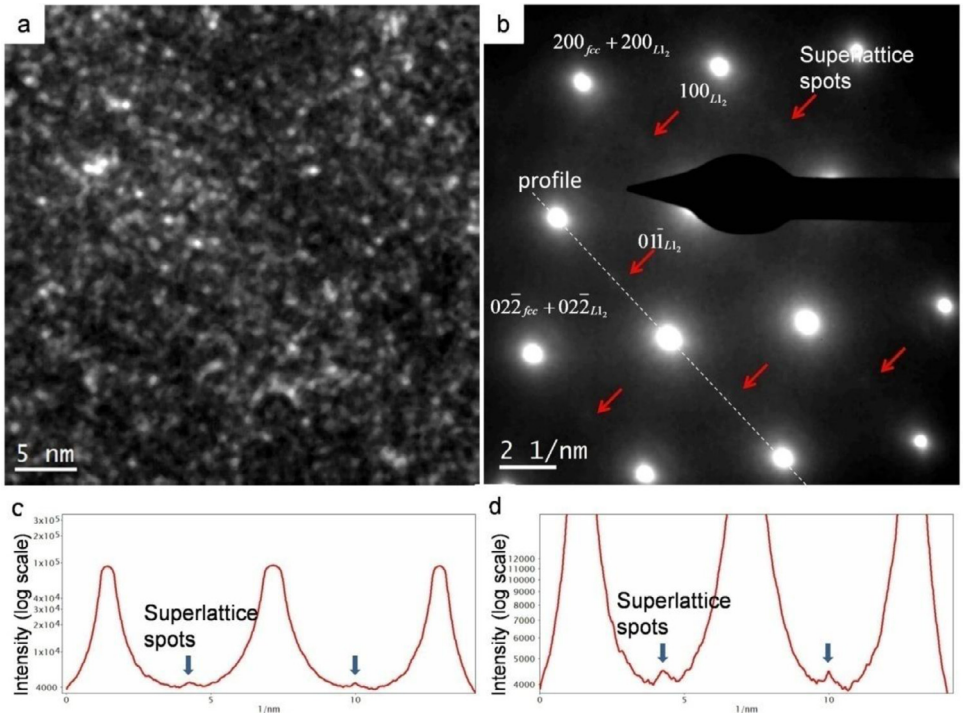

Fig. 2. TEM characterization of LRO $L1_2$ domains in $(CrCoNi)_{93}Al_4Ti_2Nb$ alloy: (a) dark field TEM image; (b) corresponding selected area diffraction pattern along [011] zone axis of the FCC matrix phase; (c) intensity profile along the white dash line highlighted in (b); and (d) enlarged view of the intensity profile shown in (c).

they are included, the average grain size is 11 μm. The texture IPF map constructed for the crystal direction along the tensile direction in Fig. 1b indicates that there are weak <111> and <100> fiber textures in the test material, which are typical textures observed in FCC alloys after cold rolling followed by annealing [57].

Fig. 2a is a dark field TEM image revealing very fine $L1_2$-type long range ordering (LRO) domains in the microstructure. Fig. 2b shows the corresponding selected area diffraction pattern recorded along [011] zone axis of FCC matrix. Very faint superlattice reflections can be seen in the pattern, indicating the formation of LRO $L1_2$ domains. To more clearly view the superlattice reflections, the intensity profile across diffraction spots highlighted using the white dash line in Fig. 2b are given in Fig. 2c. Fig. 2d is an enlarged view of the intensity profile to reveal the weak superlattice diffraction from LRO $L1_2$ domains. Fig. 3a and d are atomic resolution HAADF-STEM images along [001] and [011] zone axes of the FCC matrix phase, respectively. The inset fast Fourier transform (FFT) patterns in Fig. 3a and d clearly show the {001} and {011} superlattice intensities from $L1_2$ domains. To more clearly reveal these $L1_2$ ordering domains in the HAADF STEM images, inverse FFT (IFFT) images were obtained only using superlattice reflections, as shown in Fig. 3b and e. Several methods for filtering these reflections (e.g. annular masks versus aperture masks) were assessed, with similar results obtained. As shown in Fig. 3b and e, the spatially-localized LRO $L1_2$ domains have an interconnected morphology, which is often observed in spinodal decomposition. The average size of LRO $L1_2$ domains measured using IFFT images is about 3.1 nm. Cross-correlation image processing [58] was conducted to better show the LRO $L1_2$ domains. The inverse FFT images in Fig. 3b and 3e were processed through cross-correlation using the motif of ordered $L1_2$ unit cells. Fig. 3c and f are corresponding images after cross-correlation processing. As compared with inverse FFT images

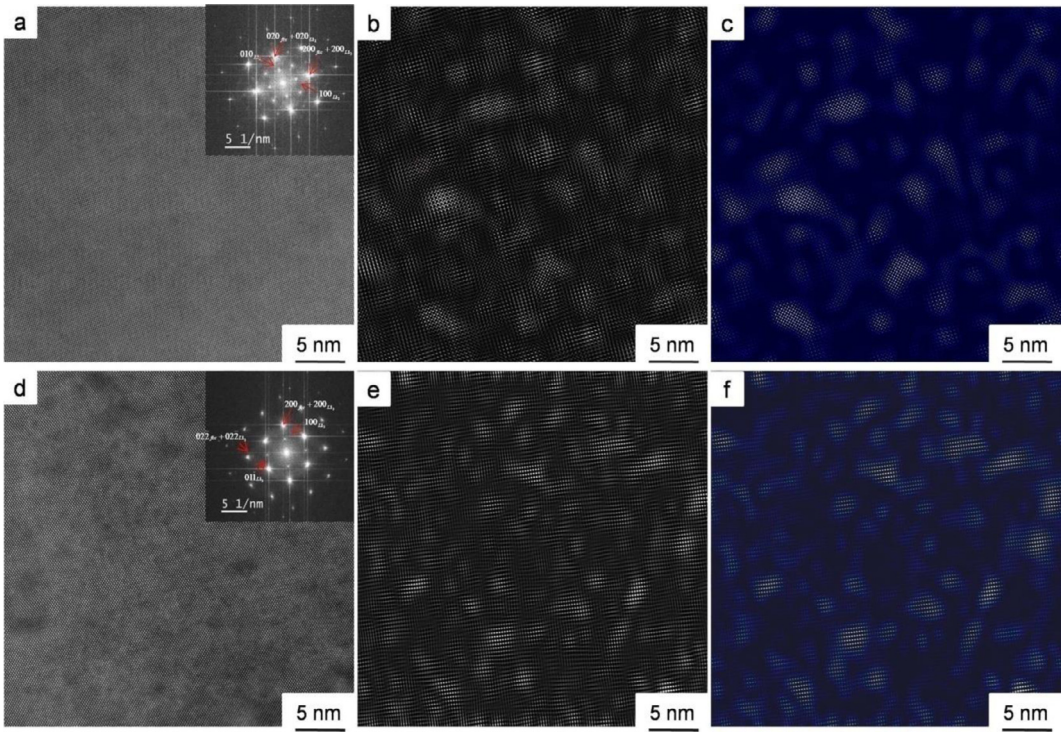

Fig. 3. Atomic resolution HAADF-STEM imaging of LRO $L1_2$ domains in $(CrCoNi)_{93}Al_4Ti_2Nb$ alloy: (a) HAADF-STEM image along [001] zone axis of the FCC matrix phase; (b) IFFT image of Fig. 3a using {010} and {100} superlattice reflections of LRO $L1_2$ domains; (c) IFFT image after cross-correlation processing; (d) HAADF-STEM image along [011] zone axis of the FCC matrix phase; (e) IFFT image of Fig. 3d using {100} and {011} superlattice reflections of LRO $L1_2$ domains; and (f) IFFT image after cross-correlation processing.

in Fig. 3b and e, the inverse FFT images after cross-correlation processing demonstrate some improvement in displaying the LRO $L1_2$ domains in the microstructure.

Previous studies show that under very high cooling rates such as during quenching or rapid solidification, ordered $L1_2$- γ' domains can be formed by spinodal decomposition [59–64]. This early stage of LRO may form within compositional pockets created by a preceding phase separation via spinodal decomposition within the parent FCC solid solution. The distribution of alloying elements in the solution treated and quenched alloy was characterized using atom probe tomography (APT). Fig. 4a shows the reconstructed 3D ion maps of all elements in the alloy. Based on these ion maps it is difficult to discern any compositional clustering in this alloy. However, based on the electron microscopy evidence of LRO $L1_2$ domains in the microstructure, the APT results were analyzed in detail to carefully investigate possible compositional heterogeneities at the nanometer scale. The Ti iso-concentration surface shown in Fig. 4b reveals the regions rich in Ti (>2.3 at%). These Ti-rich regions appear to be interconnected in nature, in agreement with the HAADF-STEM characterization, and indicate the early stages of a spinodal decomposition [62,63]. The corresponding proximity histograms (or compositional profiles), shown in Fig. 4c, further reveal that these regions are also rich in Ni, Al and Nb, consistent with previously reported partitioning trends between γ and γ' [65]. While these compositional partitioning trends can be assessed using the proximity histograms, shown in Fig. 4c, it is not possible to get an accurate measurement of the Ni, Al, Ti enriched domains based on these profiles. Therefore, additional analysis of these domains was carried out using cluster analysis specifically for the γ' stabilizing elements (Ni, Al, Ti). Fig. 4d shows an example of a typical 3D volume used for identifying ordering domains. Fig. 4e shows the 3D reconstruction of domains enriched in Ni, Al and Ti calculated using the cluster searching algorithms available in IVAS 3.8.4. The method used was the maximum separation method [55,56]. The average composition of ordering domains is given in Table 1. As compared with the nominal compositions of the alloy, the LRO $L1_2$ domains exhibit a higher concentrations of γ' forming elements (Ni, Al and Ti), and low concentrations of γ forming elements (Cr and Co). The compositions of γ' precipitates in this alloy at different equilibrium temperatures were calculated using the Thermo-Calc^{TM} software coupled with a TCNI 8.2 database. The calculated equilibrium compositions of γ' precipitates at 1000°C and 20°C are also listed in Table 1 for comparison with the compositions of the LRO domains. It can be seen that the compositions of the LRO $L1_2$ domains deviate from those of γ' precipitates at equilibrium compositions. The Thermo-Calc^{TM} TCNI 8.2 database used in the calculation may not be able to accurately predict the compositions of $L1_2$ precipitates because the composition of $(CrCoNi)_{93}Al_4Ti_2Nb$ alloy lies close to the center of Ni-Co-Cr phase diagram. This may be one possible reason for the large difference between the measured composition of LRO domains and the equilibrium composition of γ' precipitates. Another possible reason is that the ordering process may be only partially completed due to the limited time for diffusion in water quenching. CALPHAD calculations only predict the equilibrium composition of γ' precipitates. This partial ordering process may also contribute to the large observed difference in compositions between LRO domains and equilibrium $L1_2$ γ' precipitates. The average size of the LRO $L1_2$ domains is about 4 nm based on APT results, which is close to the average size measured using HAADF STEM imaging (~3.1nm). The compositions of ordered γ' domains formed in spinodal decomposition can be quite different from the equilibrium γ' phase [62,63], consistent with the results shown in Table 1.

3.2. Tensile response

Fig. 5a compares the engineering stress-strain curve of $(CrCoNi)_{93}Al_4Ti_2Nb$ alloy with that of CrCoNi alloy from an early

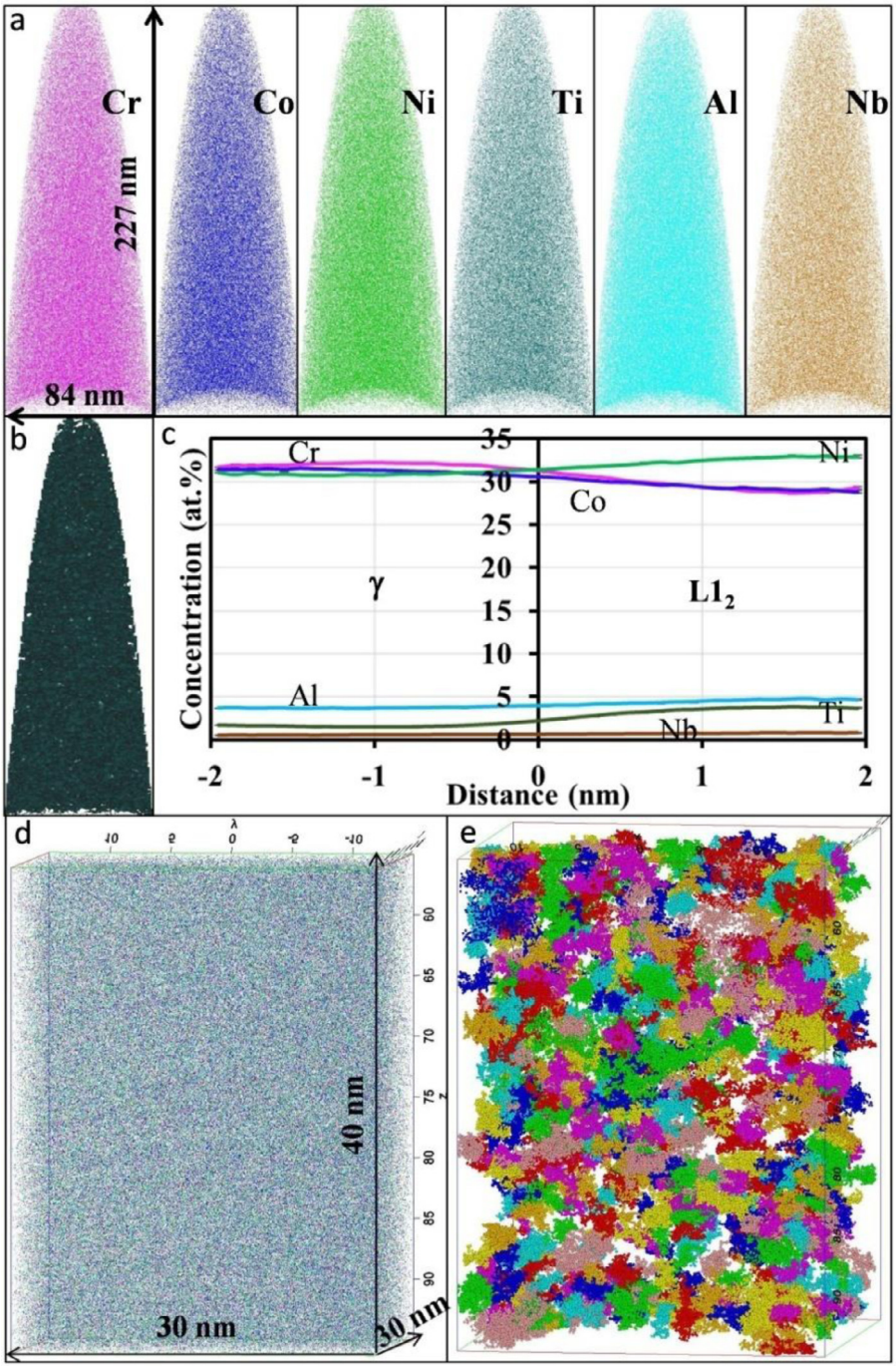

Fig. 4. APT characterization of the microstructure of the test alloy: (a) 3D ion maps of all elements; (b) Ti 2.31 at.% iso-surface reveals the interconnected Ti-rich regions; (c) Proxigrams of all elements showing the enrichment of Ni, Al, Ti and Nb in $L1_2$ ordering domains; (d) 3D view of the volume searched for ordering or clustering; and (e) 3D reconstructed volume showing the domains enriched with γ' formers (Ni, Ti and Al). Colors represent identified clusters.

Table 1
Average compositions (at.%) of LRO $L1_2$ domains measured by APT as compared with the nominal composition of the alloy and the equilibrium compositions of γ' phase at 1000 °C and 20°C calculated using Thermo-Calc software.

	Ni	Co	Cr	Al	Ti	Nb
Nominal alloy composition	31.0	31.3	30.6	4.1	2.3	0.9
Measured composition of LRO $L1_2$ domains	51.3	19.42	19.1	6.4	3.41	0.37
Equilibrium composition of γ' precipitate at 1000°C (CALPHAD)	58.46	14.47	2.57	10.92	11.52	2.04
Equilibrium composition of γ' precipitate at 20°C (CALPHAD)	74.80	0.20	0.02	7.90	14.02	3.05

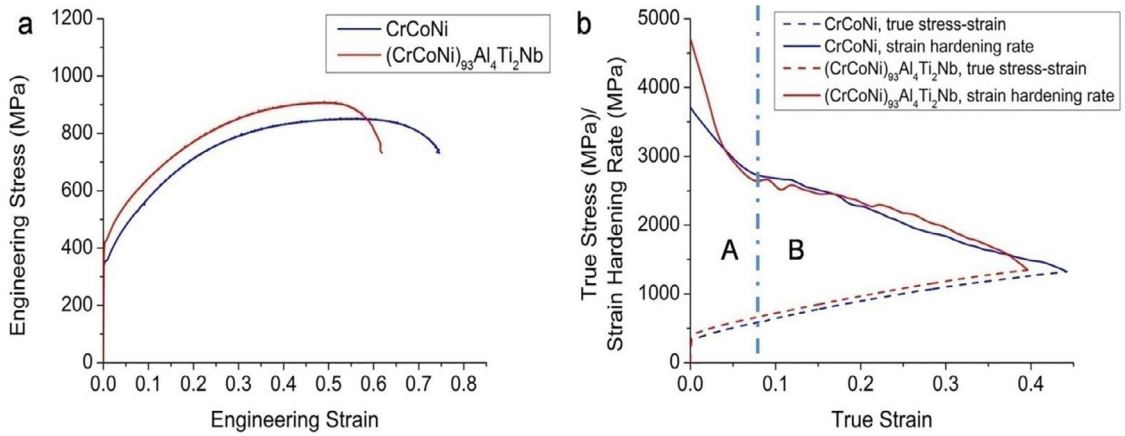

Fig. 5. Tensile properties and strain hardening rate curve of $(CrCoNi)_{93}Al_4Ti_2Nb$ as compared with those of CrCoNi [53]: (a) engineering strain-stress curves; and (b) strain hardening rate curves and true stress-strain curves.

study [53].The average grain size of the CrCoNi alloy is about 24 μm, which is close to that of $(CrCoNi)_{93}Al_4Ti_2Nb$ alloy (~26μm). It can be seen that $(CrCoNi)_{93}Al_4Ti_2Nb$ has a slightly higher yield strength (about 70 MPa higher). Fig. 5b show the strain hardening rate and true stress-strain curves of $(CrCoNi)_{93}Al_4Ti_2Nb$ as compared with those of CrCoNi. The strain hardening rate curve can be divided into two stages as indicated in Fig. 5b. Small serrated features in the strain hardening rate curves of $(CrCoNi)_{93}Al_4Ti_2Nb$ and CrCoNi are mainly due to experimental noises and they have no large effects on the overall trend of strain hardening rate curves. In stage A, up to plastic strains of about 8%, the strain hardening rate decreases rapidly with increasing deformation, which is normally observed in FCC based alloys. In stage B, the strain hardening rate continues to decrease with increasing plastic deformation, but less rapidly than in stage A. The strain hardening behavior of $(CrCoNi)_{93}Al_4Ti_2Nb$ is similar to that of CrCoNi. Two alloys have similar uniform elongation (ductility) as shown in Fig. 5b. Detailed characterization of deformation microstructures at different stages of strain hardening will be given in the following section.

3.3. Evolution of deformation substructures

The evolution of deformation microstructure at different plastic strain levels was characterized using EBSD. Figs. 6a-d show the IPF maps of the microstructure after 0.6%, 3%, 12% and 62% engineering strain. Figs. 6e-h show the corresponding kernel average misorientation (KAM) maps. With increasing of strain, dislocation density increase within the grain as shown in the KAM maps. Fig. 6i is an image quality map showing the microstructure after deformation to 62% engineering strain. Misorientation along the line highlighted in Fig. 6i was analyzed and presented in Fig. 6j. Both point-to-point and point-to-origin misorientation analysis reveal the formation of low angle boundaries within grain interiors due to plastic deformation. EBSD characterization at all stages did not reveal the formation of deformation twins.

ECCI images in Fig. 7 show the evolution of deformation substructures at different stages of plastic deformation. Fig. 7a shows main features of dislocations after 0.6% strain. Dislocation slip has a strong planar character and dislocations are localized within individual slip bands. Fig. 7b shows that planar slip bands from different slip systems intercept each other. With further increase of plastic deformation, the spacing between slip bands continues decreasing as shown in Fig. 7c. Fig. 7d shows the deformation substructures after testing up to 62% strain. High density of dislocations and very fine slip bands can be observed in Fig. 7d.

To further study dislocation substructures and its evolution at different stages of plastic deformation, TEM specimens were extracted from interrupted test specimens as well as from a tensile specimen tested to fracture. Scanning transmission electron microscopy (STEM) coupled with conventional transmission electron microscopy (TEM) was used to characterize the dislocation substructures. Zone axis bright field STEM images along the [101] zone axis of the FCC matrix phase in Fig. 8 reveal the evolution of dislocation substructures at four different deformation levels. Fig. 8a shows the dislocation substructure after 0.6% plastic deformation. Dislocation slip has pronounced planar character and dislocations are mainly constrained within slip bands on {111} slip planes. Upon further straining to 3% strain, the number of slip bands increases, and dislocation density increases rapidly, but most dislocations are still constrained within planar slip bands as shown in Fig. 8b.The interaction of slip bands from different slip systems divides the grain into subgrain structures. One significant difference between the dislocation substructure of $(CrCoNi)_{93}Al_4Ti_2Nb$ and CrCoNi is that few extended dissociated dislocations are observed in the former, while a high density of extended dissociated dislocations is observed in CrCoNi after 6.3% strain [13]. Those extended dissociated dislocations play a critical role in deformation twinning and plasticity induced FCC-HCP transformation in CrCoNi alloy [13]. With further increase of plastic deformation up to 12% strain (Fig. 8c), the density of slip bands increases and grains are further refined by slip bands. Fig. 8d shows the deformation microstructure after testing to rupture (62% strain). It can be seen that a very high density of dislocations is uniformly distributed in the microstructure. A high density of slip bands is still observed in the microstructure. Dislocations tend to lose the planar slip character and form more tangled structures. The inset selected area diffraction pattern in Fig. 8d shows the absence of extra spots from deformation twins, indicating no deformation twins form during tensile testing. This has been confirmed by observing multiple grains since the occurrence of deformation twinning depends on grain orientations [66].The main features of deformation substructure at different stages of deformation revealed by ECCI imaging in Fig. 7 are consistent with those observed using STEM imaging in Fig. 8.

To further understand the evolution of the deformation microstructure, detailed characterization of dislocations was performed on TEM specimens extracted from a specimen interrupted at 0.6% strain. To reveal the dissociated dislocations in the specimen and measure dissociation distances, the recently developed weak beam dark field STEM imaging techniques were used [54]. The analysis was conducted on one TEM foil with the normal

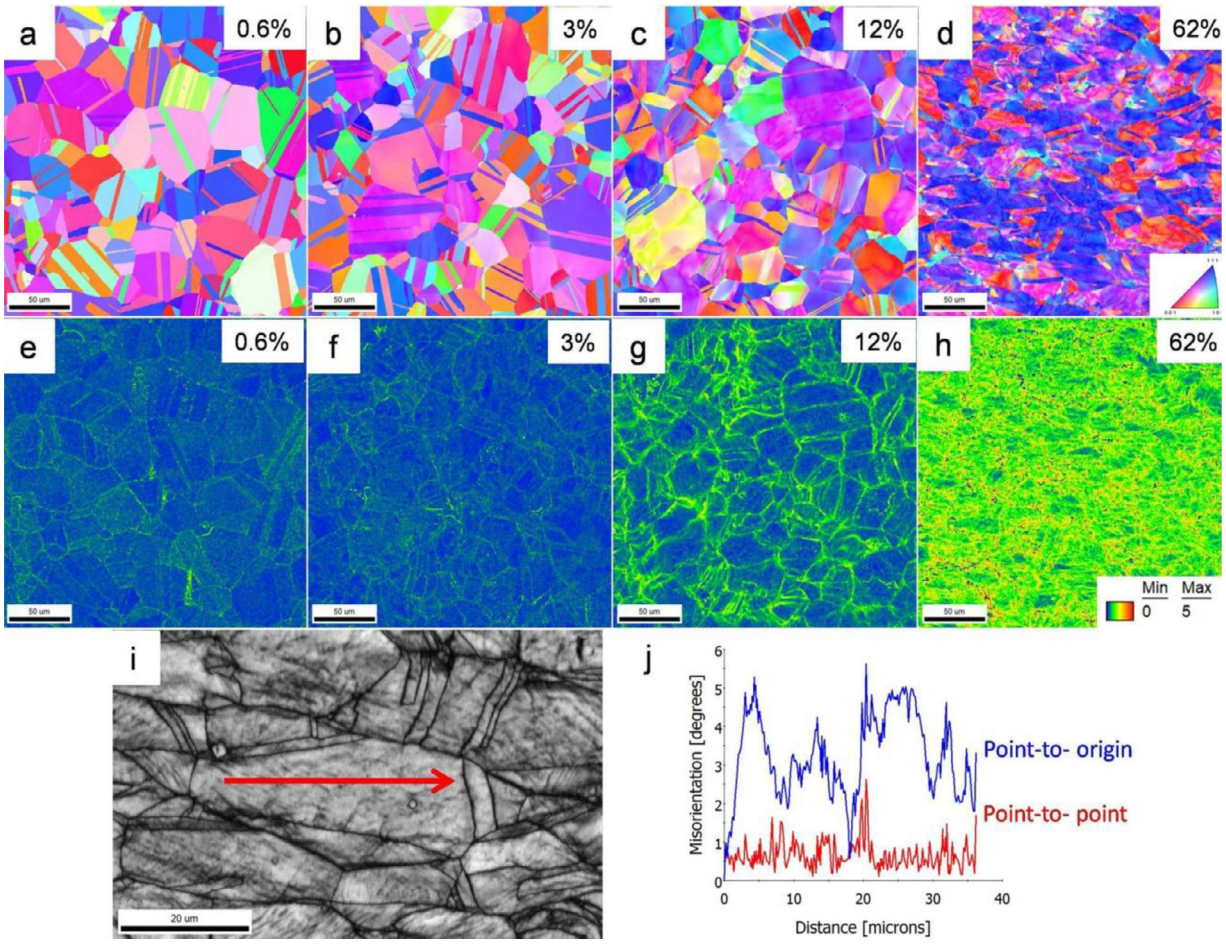

Fig. 6. EBSD characterization of the evolution of deformation substructures with plastic deformation: (a)-(d) IPF map at different strain levels; and (e)-(h) corresponding KAM maps at different strain levels; (i) image quality map of the microstructure after 62% strain (red line highlights the location for misorientation analysis shown in (j); and (j) point-to-origin and point-to-point misorientation analysis along the line highlighted in Fig. 6i.

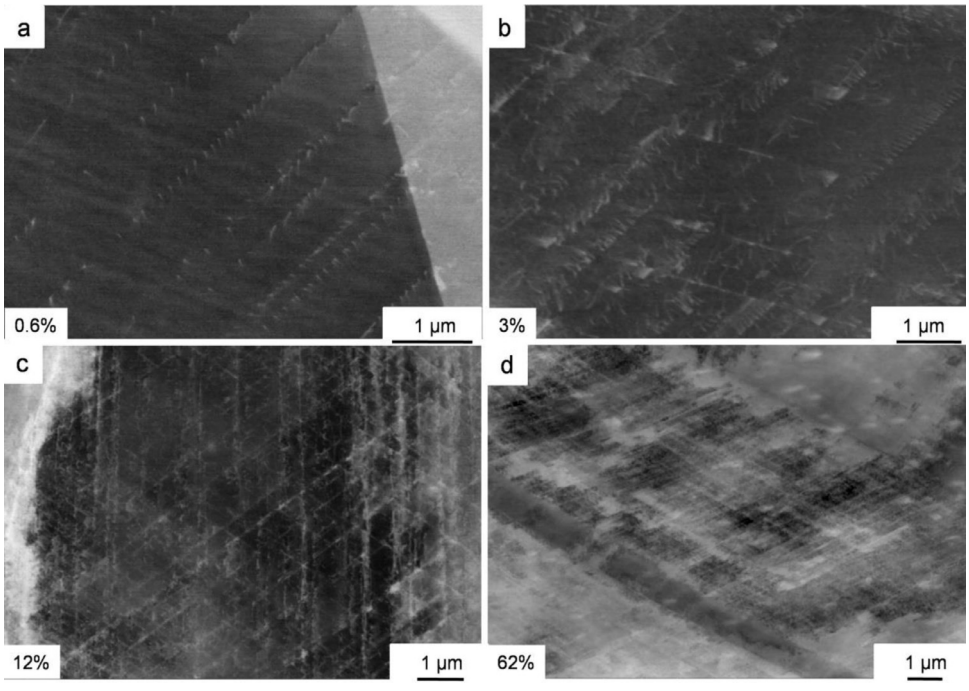

Fig. 7. ECCI characterization of deformation substructures at different stages of plastic deformation: (a) 0.6% strain; (b) 3% strain; (c) 12% strain; and (d) 62% strain.

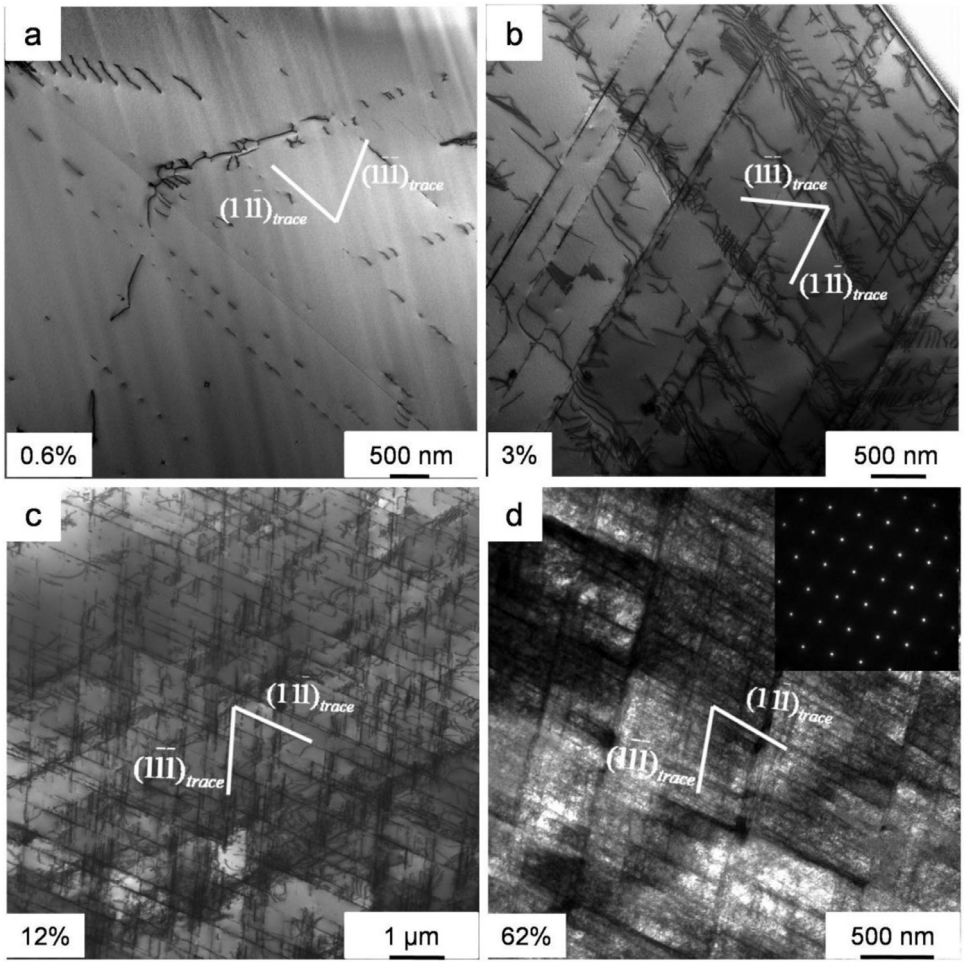

Fig. 8. Bright field [101] zone axis STEM images of deformation substructures at different stages of plastic deformation: (a) 0.6% strain; (b) 3% strain; (c) 12% strain; and (d) 62% strain.

direction close to the [111] direction. In FCC alloys with low stacking fault energy, a full dislocation with a Burgers vector of a/2<110> will dissociate into two $a/6\langle\bar{1}\bar{1}2\rangle$ Shockley partial dislocations bounding a stacking fault. Dislocation visibility and invisibility based on $g \cdot b$ analysis was performed using WB DF STEM method to identify the Burgers vectors of partial dislocations and full dislocations. Fig. 9 shows an example of WB DF STEM imaging of a dissociated dislocation using three different $3g_{\{220\}}$ types of diffraction conditions. The dissociated dislocation is on the (111) slip plane, which is also close to the foil plane in this case. Under $3g_{(\bar{2}02)}$diffraction condition, both partial dislocations are visible in Fig. 9c, while the stacking fault contrast is invisible. Based on the $g \cdot b$ analysis, the Burgers vector of two partial dislocations and the full dislocation were identified and labeled in Fig. 9. This portion of the full dislocation has near edge character. The dissociation distance between two partial dislocations is about 9 nm. The high magnification image in Fig. 9d shows the details of the dissociated dislocation. Similar characterization and measurement of dissociation distances were conducted on other dislocations. The results are summarized in Fig. 10. The dissociation distances of dislocations in the equiatomic CrCoNi at room temperature were also measured using the same weak beam dark field STEM technique, and the results are included in Fig. 10 for comparison. It can be seen that the dissociation distances in the CrCoNi are much larger than those in $(CrCoNi)_{93}Al_4Ti_2Nb$. Theoretical dissociation distances as a function of dislocation characteristic angles and SFE were also calculated and are shown in Fig. 10. The shear modulus of $(CrCoNi)_{93}Al_4Ti_2Nb$ is assumed to be equal to that of CrCoNi in the calculation, which is 87 GPa [10]. Through fitting the experimental measurements to the theoretical calculated results, the stacking fault energy of $(CrCoNi)_{93}Al_4Ti_2Nb$ alloy is estimated to be around 25 mJ/m^2 which is higher than that of the CrCoNi alloy, which is about 16 mJ/m^2.

Zone axis bright field STEM images in Fig. 11 show the main features of dislocations in $(CrCoNi)_{93}Al_4Ti_2Nb$ alloy after 0.6% plastic strain. The primary $[011](1\bar{1}1)$ slip system in the grain has the highest Schmid factor of 0.49, while the slip system $[01\bar{1}](111)$ has a Schmid factor of 0.45. As shown in the figure, both slip systems operated under loading. Dislocation slip has a strongly planar character. Most dislocations are localized within {111} slip bands. Two distinct dislocation configurations are observed in Fig. 11: paired dislocations and dislocation multipoles. Fig. 11b shows two slip bands consisting of paired dislocations on the same $(1\bar{1}1)$ slip plane. The two slip bands originated from opposite directions. The distance between the leading dislocation pair is smallest and the distance between following paired dislocations increases. The formation of paired dislocations indicates the existence of short range ordering (SRO) or very fine-scale precipitates or ordering domains. Paired dislocations have been frequently observed in the deformation of nickel-based superalloys [67–71] and alloys with short - range ordering or long range ordering [72–74]. Due to the LRO $L1_2$ domains in the present alloy, slip occurring by the movement of a $a/2\langle110\rangle$ full FCC matrix dislocation through the ordered structure will result in the formation of anti-phase boundaries, which

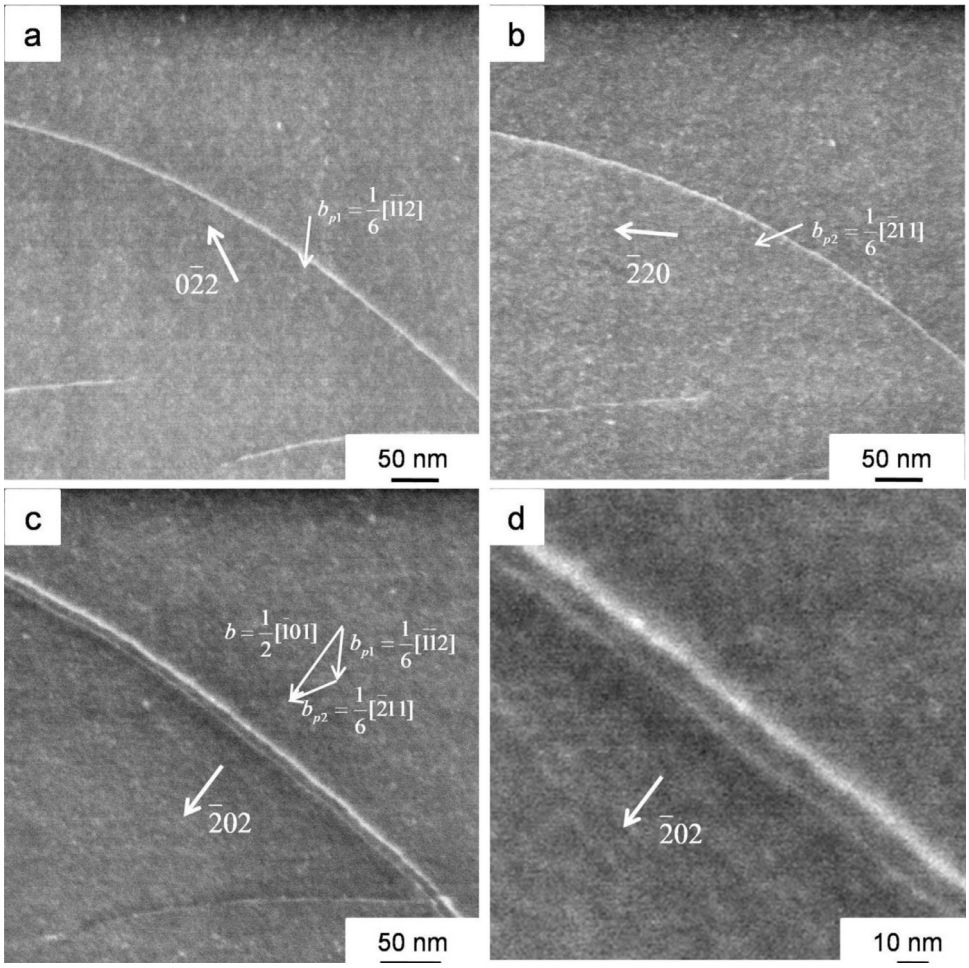

Fig. 9. Weak beam dark field STEM characterization of a dissociated dislocation using three different diffraction vectors: (a) image with a diffraction vector of $3g_{(0\bar{2}\bar{2})}$; (b) image with a diffraction vector of $3g_{(\bar{2}\bar{2}0)}$; (c) image with a diffraction vector of $3g_{(\bar{2}02)}$; and (d) high magnification image of the dissociated dislocation.

are unfavorable high energy configurations. Full dislocations in the LRO $L1_2$ domains have a Burgers vector of $a\langle 110\rangle$. Therefore, the movement of the second $a/2\langle 110\rangle$ full FCC matrix dislocation will restore the structure within the ordering regions. The distance between nearby dislocations within the slip bands consisting of paired dislocations were measured. Fig. 12 shows the measurement results of four slip bands. The method used in measuring is illustrated and inserted in Fig. 12. It reveals that the distances between the first five paired dislocations have similar values in all four slip bands. The average distance between dislocations in the first paired dislocation is about 19 nm. There is no large difference in distances between unpaired dislocations in four slip bands. The fact that the pairing persists only for several sets of dislocations is indicative of a short-range ordered condition [34,72,75], or very fine-scale long range ordered structures [19,67–71].

Fig. 11c shows an example of the second type of dislocation configuration: a multipole within a slip band. The multipoles are formed from dislocations with opposite signs on adjacent slip planes. They represent a low energy dislocation configuration and can act as obstacles to slip for subsequent dislocations within the same slip bands [76], thus contributing to strain hardening [77]. Fig. 11d shows another example of the multipole structure. This multipole was formed by dislocations on the $(1\bar{1}1)$ slip plane. It interacts with and blocks dislocation slip on the (111) slip plane as shown in Fig. 11d. Those multipoles retard dislocation slip within grains, serving as building blocks for the formation of refined subgrain structures observed in Fig. 8c.

Fig. 13 shows weak beam dark field STEM images of dislocations in the slip bands shown in Fig. 11b. The images were acquired using different diffraction vectors. Both slip bands (labeled 1 and 2) included in Fig 11 are on $(1\bar{1}1)$ planes. In Fig. 13a, under a diffraction vector of $3g_{(002)}$ of the FCC matrix, only partial dislocations with a Burger vector of $a/6[\bar{1}12]$ are visible in the slip bands. When imaging with a diffraction vector of $3g_{(0\bar{2}\bar{2})}$, both partial dislocations are visible as shown in Fig. 13b. The dislocations within slip band 1 have a Burgers vector of $a/2\ [0\bar{1}\bar{1}]$, while the dislocation in the nearby slip band 2 has an opposite Burgers vector of $a/2[011]$ as indicated in Fig. 13c. The "sign" of the Burgers vector can be deduced from the swapping of "strong" and "weak" partial contrast in the two bands. This asymmetry in contrast is expected under weak-beam conditions based on numerous previous studies using conventional diffraction contrast imaging [21,22,78], and also applies to the new weak beam dark field STEM conditions. Note that in slip band 1, the partial with "strong" contrast is the lower partial dislocation, while in slip band 2, the contrast of the upper partial dislocation appears "stronger". The opposing sign of the dislocations in these two arrays is also consistent with the apparent distribution of dislocation spacings in the two bands, which can be readily seen in Fig. 11b.

The higher magnification weak beam dark field STEM image in Fig. 13d shows the fine features of the dissociated dislocations. The full dislocations are narrowly dissociated into two partial dislocations. The dissociation distances vary considerably along the dissociated dislocation lines. Previous atomistic simulation has shown

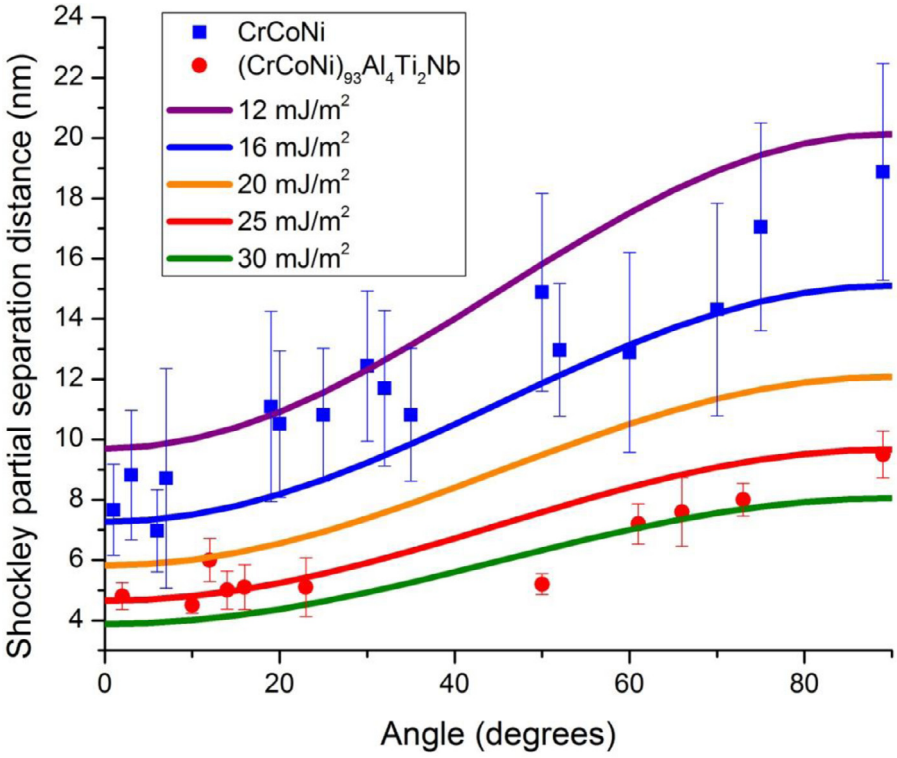

Fig. 10. Measured dissociated distances in $(CrCoNi)_{93}Al_4Ti_2Nb$ alloy as compared with those in the equiatomic CrCoNi alloy. The curves show calculated results for the indicated stacking fault energies.

local ordering in CrCoNi alloy may lead to the variation of dissociation distance [26]. In the case of $(CrCoNi)_{93}Al_4Ti_2Nb$ alloy, interaction with local ordering regions may also accentuate the variation of dissociation distances, and in fact create potent pinning sites along the dislocations. The "leading" partial dislocation of each dissociated $a/2[011]$ dislocation appears to have a more serrated appearance than does the trailing partial. It should also be noted that the dislocation shown in Fig. 9 and those included in the data shown in Fig. 10 were for dislocations in different grains/samples that were isolated from other dislocations, that is, they were not part of dislocation arrays. This selection was intentional in order to measure dislocation dissociation without effects of dislocation interactions. The dramatically different appearance of the partials with respect to serrations in Fig. 9 versus Fig. 13 also suggest that the dislocation in Fig. 9 (and others contributing to the data in Fig. 10) was not mobile during the tensile experiment and is perhaps a dissociated dislocation that was pre-existing after processing.

The dissociation distances of paired dislocations and unpaired dislocations within slip bands were measured and some examples of measurements are shown in Fig. 14a and b. To reduce the effects of serrated features of the partials on measurement, the dissociation distance between partials were determined through dividing the dissociated area between two partials by the length of partials. The dissociated area between partials and length of partials were measured on weak beam dark field STEM images as illustrated in Fig. 14c and d respectively. The results in Fig. 14a and b indicate that the dissociation distance between partials increases with increasing distance away from the leading paired dislocations. The dissociation distance between the leading partials has a minimum value of about 4 nm. The full dislocations in the slip bands are close to edge character. The dissociation distances of weakly paired dislocations or unpaired dislocations in the slip bands are close to those measured in Fig. 10.

Bright field zone axis STEM images in Fig. 15 shows the fine substructures after 3% strain. As shown in Fig. 15a, with increasing plastic deformation, the dislocation density increases and the spacing between slip bands decreases relative to that shown in Fig. 11 (0.6% strain).The slip bands on the $(11\bar{1})$ slip plane which is edge-on in Fig. 15, divide the grain into subgrains. Slip bands on the $(1\bar{1}1)$ slip plane intercept slip bands on the $(11\bar{1})$ slip plane, leading to further partitioning of the grain. As shown in Fig. 15b, a multipole on the (111)slip plane has formed within the narrow channels of $(11\bar{1})$ slip bands. A hexagonal dislocation network was also observed on the$(1\bar{1}1)$ slip plane as indicated in Fig. 15b. All these dislocation configurations act as barriers for further slip of dislocations, thus contributing to strain hardening and accumulation of plastic deformation within grain interior. Fig. 15b shows these slip bands have two fine features. Some slip bands consist of not just single slip bands but two narrowly spaced slip bands as shown in the inset image in Fig. 15b. The spacing between the slip bands ranges from a few nm to about 20 nm. Such planar subgrain structures with narrowly spaced multiple slip bands may enhance its resistance to dislocation slip, thus contributing to work hardening capability. Another fine feature is that the slip bands are not completely continuous through the whole grain and there are frequent gaps along the slip bands as marked in Fig. 15b. The formation of those gaps is due to the heterogeneities in the dislocation content along the slip bands. Such gaps can allow slip bands from other slip systems to penetrate through and form finer subgrain structures.

Fig. 16 shows zone axis bright field STEM images revealing some fine deformation substructures after 12% strain. With increasing plastic deformation, more slip systems operate and the average spacing between slip bands continues to decrease. Dislocation slip maintains planar character. In Fig. 16a, the slip bands on the(111) slip plane and $(11\bar{1})$ slip planes are edge-on. A dislocation multipole on the$(1\bar{1}1)$ slip plane interacts with (111) slip

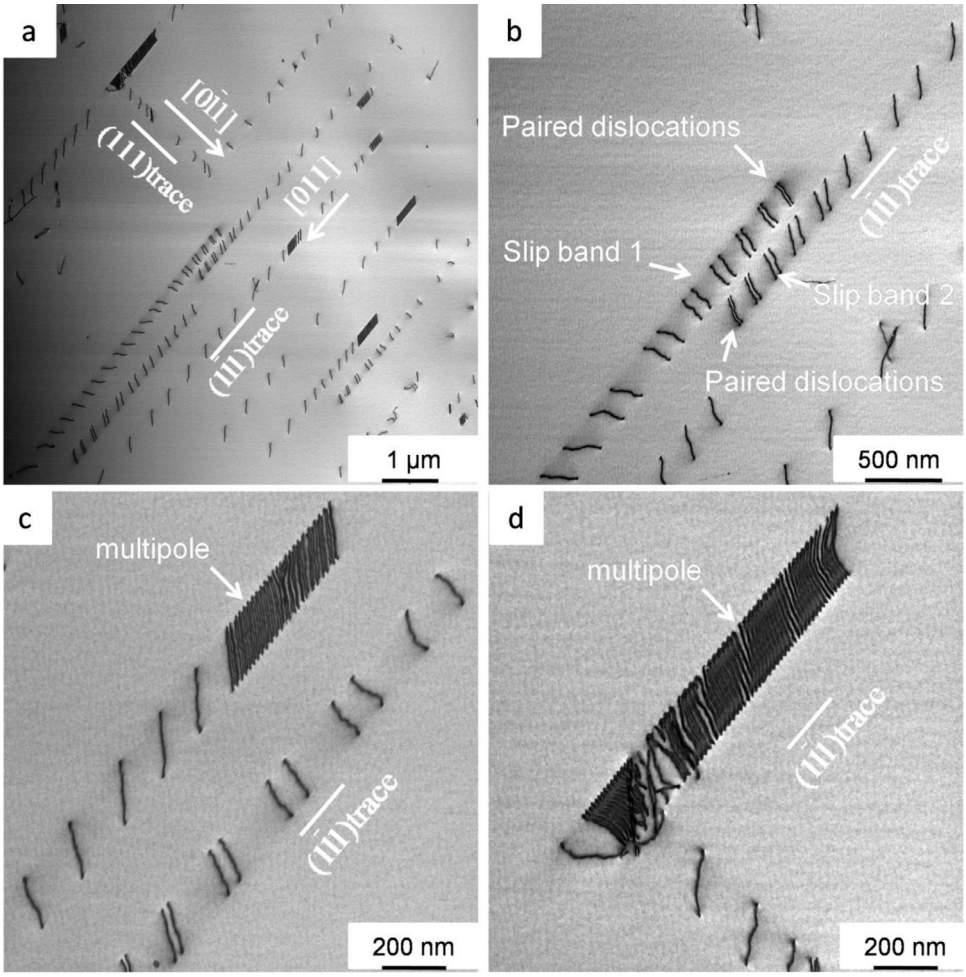

Fig. 11. [100] Zone axis bright field STEM micrographs revealing two distinct dislocation configurations: (a) low magnification image; (b) image showing paired dislocations within slip bands; (c) image showing a multipole within a slip band; and (d) image showing the interaction of a multipole on (1$\bar{1}$1) slip plane with a slip band on (111) slip plane.

bands and (11$\bar{1}$) slip bands. They may form a kind of lock structure which can further block the motion of other dislocations as indicated in Fig. 16a. Fig. 16b shows the (11$\bar{1}$) slip bands retard the slip of dislocations in a slip band on the ($\bar{1}$11) slip plane. The interactions between different slip systems further partition the grain into three dimensional subgrain structures.

4. Discussions

4.1. Ordering effects on dislocation slip characteristics

In metals and alloys, dislocation slip can generally have two different characters: planar slip and wavy slip. The present work shows that dislocation slip in $(CrCoNi)_{93}Al_4Ti_2Nb$ alloy has a strongly planar character. Two major factors are at play in creating this slip mode: low stacking fault energy and LRO domains. The alloy has a relatively low stacking fault energy of about 25 mJ/m^2. Consequently, full $a/2\langle 110\rangle$ dislocations dissociate into two $a/6\langle\bar{1}12\rangle$ Shockley partial dislocations bounding a stacking fault. Such dissociated dislocation configurations will reduce the tendency for cross-slip and thus promote planar dislocation slip.

The results of DF TEM and HAADF STEM imaging coupled with atom probe tomography indicated the existence of LRO $L1_2$ domains in the tested alloy. The LRO $L1_2$ domains are enriched in γ' forming elements (Ni, Al, Ti). The average composition of ordering domains is far from the composition of the equilibrium γ' phase, indicating that these ordering domains are in the early stages of formation through the process of spinodal decomposition [59–64]. Due to the high cooling rate and limited cooling time available during water quenching, the ordering process within LRO $L1_2$ domains may be only partially completed. This possibility is also consistent with very faint superlattice reflections in selected area diffraction patterns and the weak superlattice fringe contrast in the HAADF-STEM images. These LRO $L1_2$ domains may act as precursors for the formation of well-developed γ' precipitates during subsequent isothermal annealing [63].

The increase of planar slip tendency in alloys with short range ordering (SRO) or fine-scale long range ordering (LRO) is mainly attributed to the slip plane softening mechanism [28]. Ordered domains with different sizes act as obstacles to dislocation slip, and dislocation pairing becomes energetically favorable [19,34,67–75]. Fig. 17 schematically illustrates the slip plane softening involved in the deformation of $(CrCoNi)_{93}Al_4Ti_2Nb$ alloy. The lead dislocation in an array of dislocations emanating from a source on a {111} slip plane must cut through the distribution of LRO domains along the dislocation's length, as illustrated in Fig. 17a. After the first dislocation shears through the ordered domains, the shearing process will create high energy, unfavorable bonds on the slip plane (Fig. 17b). If the domains were fully ordered, then an anti-phase boundary (APB) would be created. The formation of high energy bonding in the APB will increase the system energy. The entry of a second dislocation with the same Burgers vector as the first dislocation

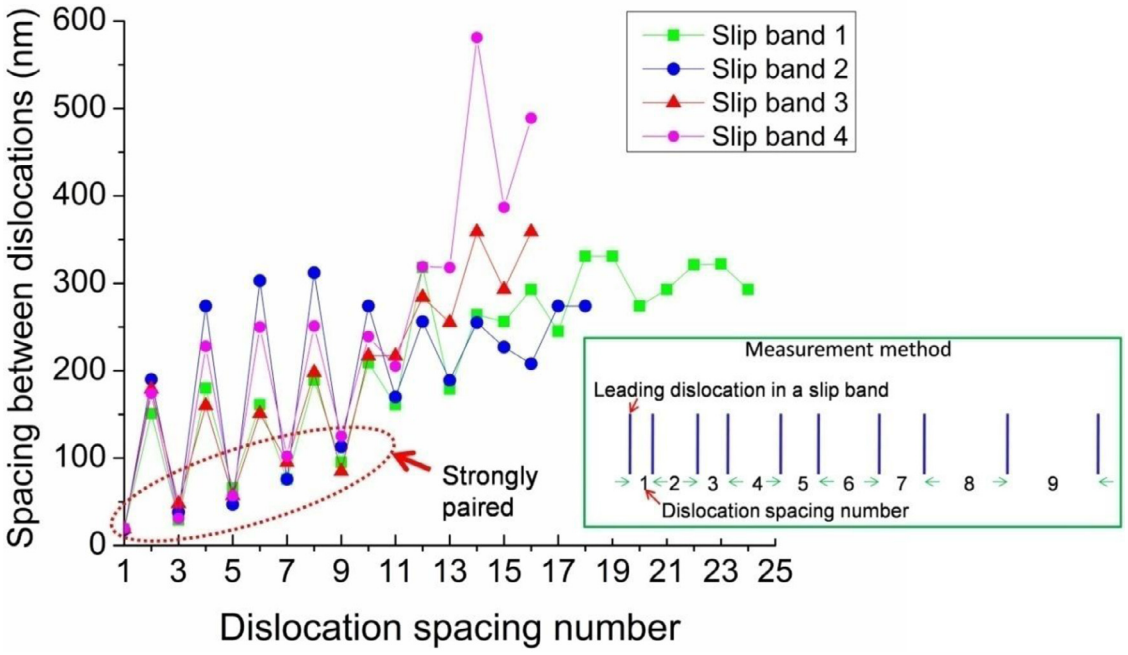

Fig. 12. Measurement of distances between the dislocations within four slip bands.

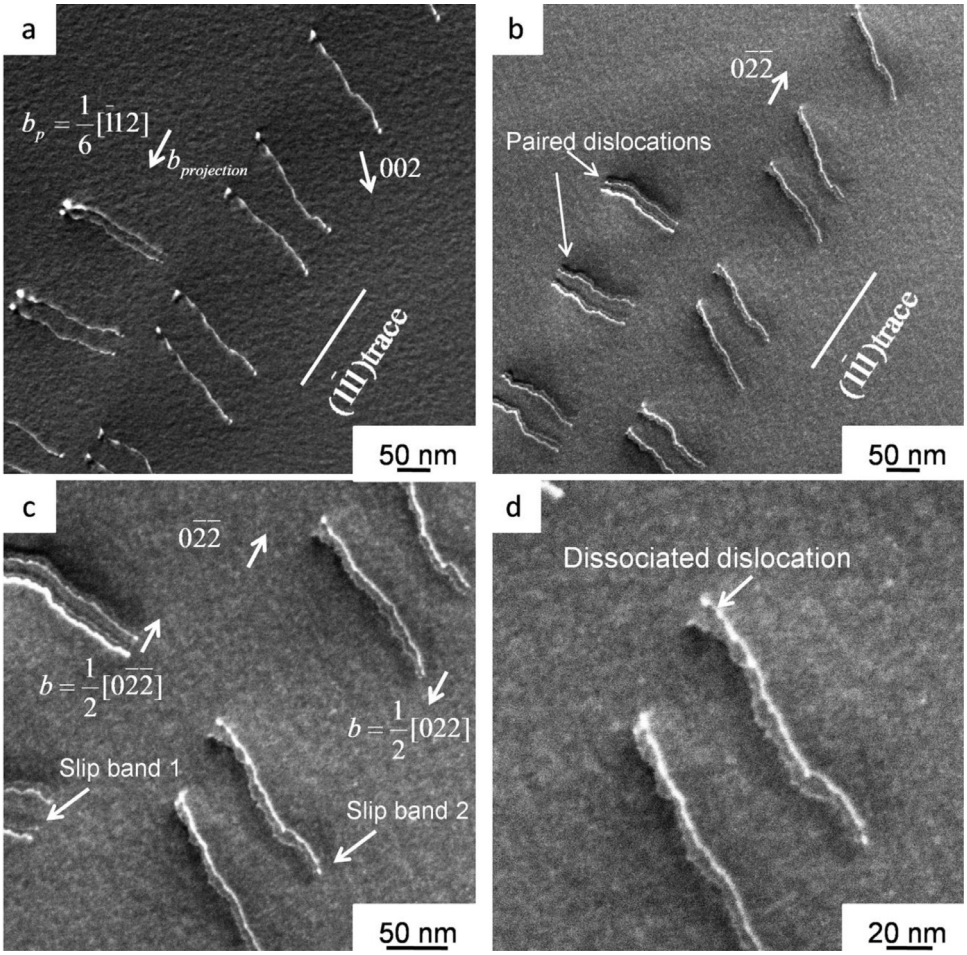

Fig. 13. Weak beam dark field STEM characterization of paired dissociated dislocations in slip bands: (a) image showing that only one of the partial dislocations is visible under a diffraction of $3g_{(002)}$; (b) image revealing both partial dislocation using a diffraction vector of $3g_{(0\bar{2}\bar{2})}$; (c) image showing dissociated dislocations within two nearby slip bands; and (d) high magnification image showing fine serrated features of dissociated dislocations in slip band 2.

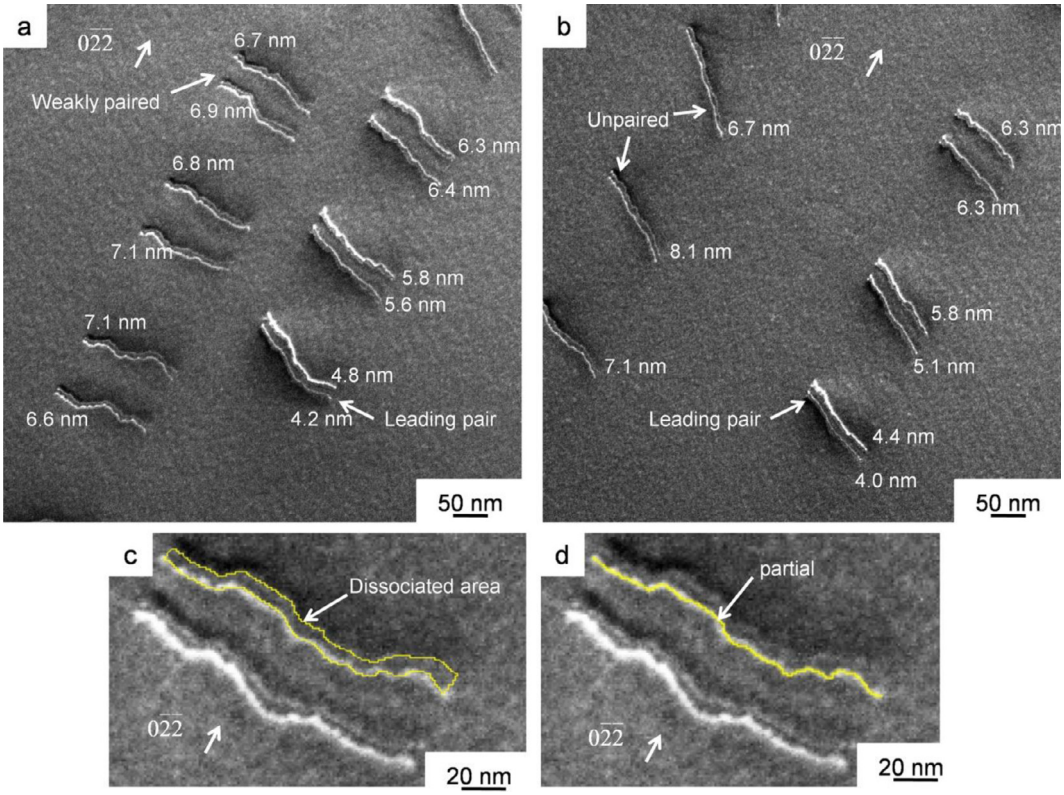

Fig. 14. Measurement of the dissociation distances of dislocations in slip bands: (a) and (b) weak beam dark field STEM images with measured dissociation distances labeled for each dislocation; (c) illustration of the measurement of the area between two dissociated partial dislocations; and (d) illustration of the measurement of the length of a partial dislocation.

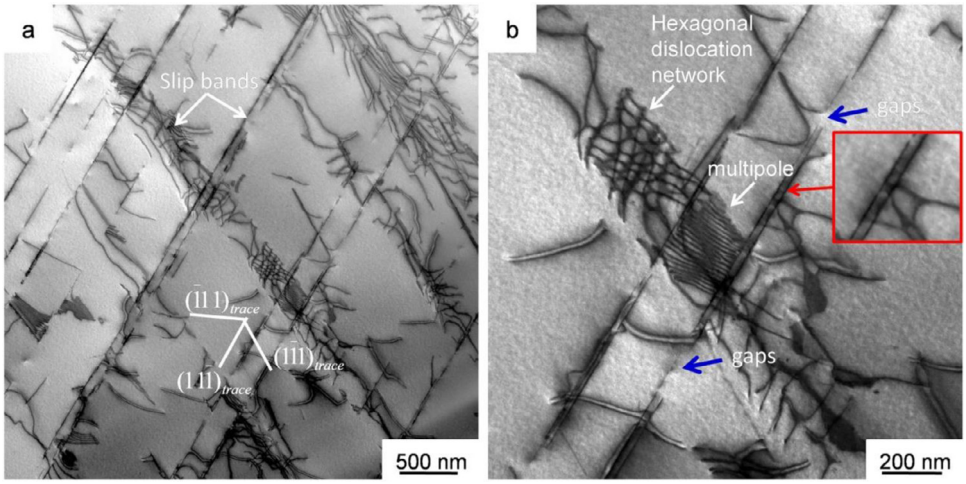

Fig. 15. Bright field [101] zone axis STEM image of deformation substructures after 3% plastic strain: (a) low magnification STEM image showing the interaction of slip bands on different {111} slip planes; and (b) STEM image showing the fine structures of slip bands (the gaps along the slip bands are highlighted using blue arrows in the figure).

is therefore energetically favorable as it will restore the bonding within the ordered region and thus reduce the system energy, as shown in Fig. 17c. Such a shearing deformation process has been frequently observed in nickel base superalloys strengthened by $L1_2$ precipitates [79,80]. After several paired dislocations slip through the LRO domains, the ordering regions will be completely sheared through. As a result, the resistance offered by LRO domains to the following dislocations will be greatly reduced and subsequent slip does not need the movement of paired dislocations, as shown in Fig. 17d. The slip of successive paired dislocations on the same slip plane leads to slip plane softening, thus promoting planar dislocation slip. The size of ordering regions can thus be estimated using the number of paired dislocations (n in Fig. 17) within one slip band multiplied by the length of the Burgers vector ($\vec{b}$ in Fig. 17) of full dislocations in the FCC matrix, which is about 0.25 nm. Such method has been used to estimate the size of ordered precipitates in Fe-Mn-Al-C steel [19]. As shown in Fig. 12, the number of paired dislocations within slip bands varies, indicating that there is a distribution in the size of spatially-localized LRO domains. The number of strongly paired dislocations is around 10 as shown in Fig. 12. Therefore, the size of LRO domains is estimated to be around 2.5 nm, which is close to the average size measured using APT (~4nm) and HAADF STEM imaging (~ 3.1nm).

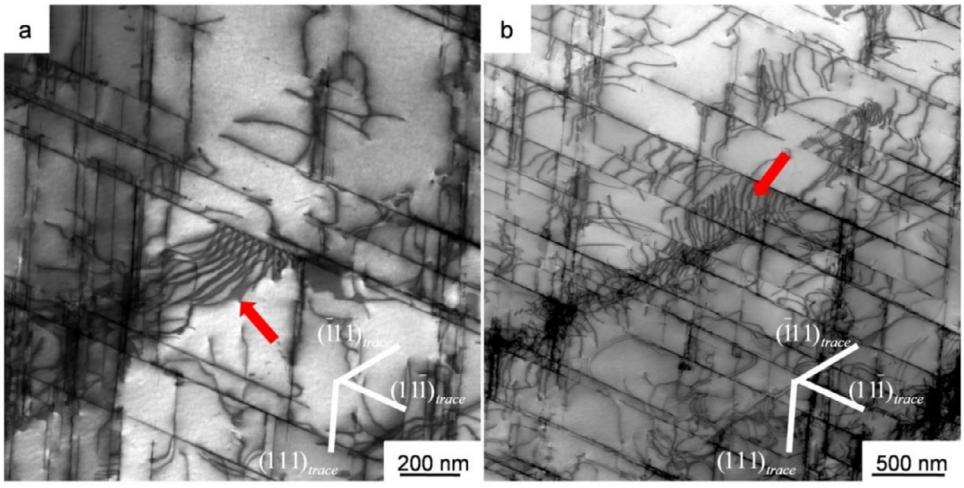

Fig. 16. Bright field [$\bar{1}10$] zone axis STEM images of the deformation substructure after 12% plastic deformation: (a) image showing the interaction between a multipole on ($1\bar{1}1$) slip plane with two edge-on slip bands; and (b) image showing the interaction of a slip band on ($\bar{1}11$) slip plane with ($11\bar{1}$) slip bands.

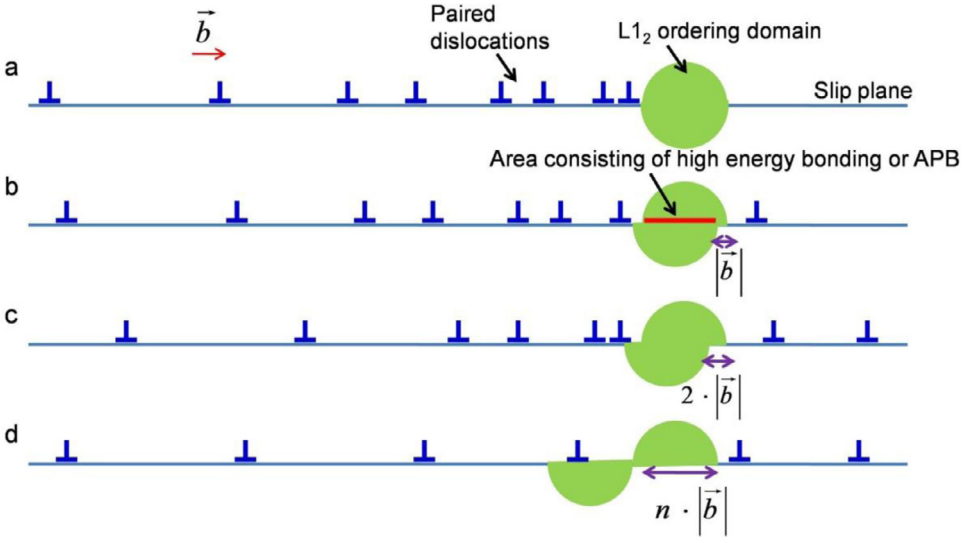

Fig. 17. Illustration of the shearing process of paired dislocations through ordered γ' domains.

Although dissociated dislocations and planar dislocation slip are observed both in CrCoNi alloy and $(CrCoNi)_{93}Al_4Ti_2Nb$, there are significant differences between their deformation mechanisms. As compared with CrCoNi [13], no largely extended dissociated dislocations are observed in $(CrCoNi)_{93}Al_4Ti_2Nb$. Furthermore, unlike in CrCoNi, no deformation twinning or deformation induced FCC-HCP transformation has been observed in $(CrCoNi)_{93}Al_4Ti_2Nb$ in the present study. Deformation twinning occurs through the slip of Shockley partial dislocations on adjacent {111} slip planes, while the transformation of FCC phase to HCP phase is achieved by the slip of partial dislocations on every other {111} slip planes [13]. Both processes involve the glide movement of extended partial dislocations. The critical twinning stress for extending stacking faults(τ^{crit}) can be estimated using the following equation [81]:

$$\tau^{crit} = \frac{2\gamma}{b_p} \tag{1}$$

Where b_p is the magnitude of the Burgers vector of Shockley partial dislocations, and γ is the stacking fault energy. For the equiatomic CrCoNi alloy, the critical twinning stress can be estimated to be 256 MPa using the measured stacking fault energy of 16 mJ/m^2 in current study, which is close to the experimentally measured result of 260±30MPa [12]. In the $(CrCoNi)_{93}Al_4Ti_2Nb$ alloy, extending of stacking faults to form twinning may involve the formation of complex stacking fault (CSF)-like structures due to the existence of LRO L1$_2$ domains. The critical twinning stress may be evaluated using the following equation modified from Eq. 1:

$$\tau^{crit} = \frac{2\gamma_m f_m + 2\gamma_{ord} f_{ord}}{b_p} \tag{2}$$

Where γ_m is the stacking fault energy of the FCC matrix, f_m is the area fraction of the matrix in the dissociated area between two partials, γ_{ord} is the complex stacking fault energy in the ordered domains, and the f_{ord} is the area fraction of the ordering domains within the dissociated area. In current study, the complex stacking fault energy and the area fraction of ordering regions in the dissociated areas is unknown. It should be pointed out that the measured stacking fault energy of $(CrCoNi)_{93}Al_4Ti_2Nb$ in this study may be treated as an average stacking fault energy which takes into account both the contribution from the FCC matrix phase and ordering regions. The critical twinning stress for $(CrCoNi)_{93}Al_4Ti_2Nb$ estimated using the measured stacking fault energy of 25 mJ/m^2 is about 400 MPa, which is much higher than that of the equiatomic CrCoNi. The equivalent stress for twinning in $(CrCoNi)_{93}Al_4Ti_2Nb$ can be estimated to be 1240 MPa when a Taylor factor of 3.1 (estimated using EBSD results) is used in the

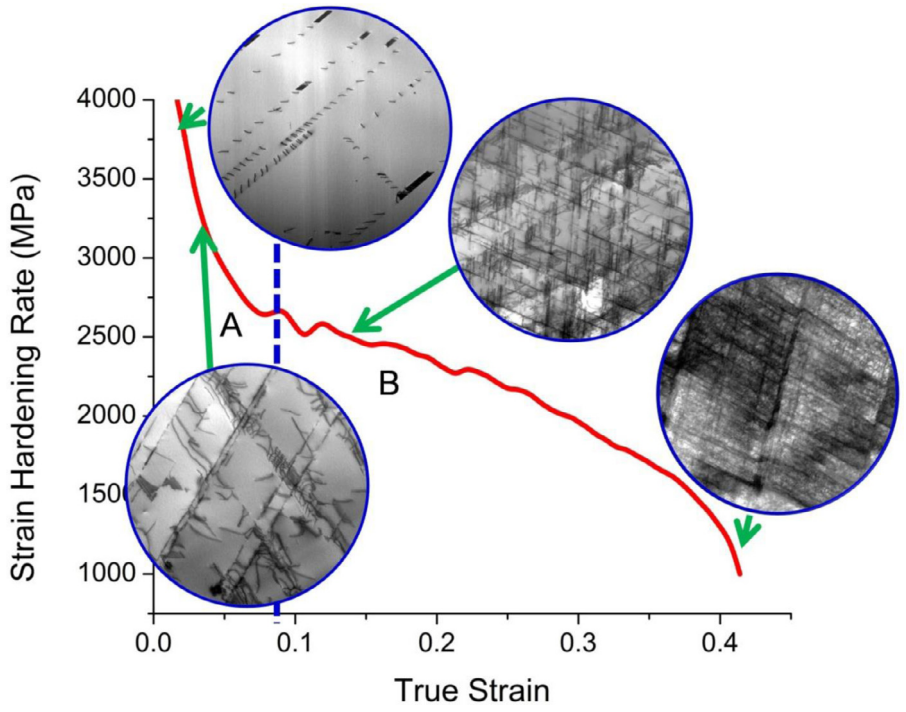

Fig. 18. Evolution of dislocation substructures at different stages of strain hardening in $(CrCoNi)_{93}Al_4Ti_2Nb$.

calculation. This equivalent stress for twinning is close to the alloy's ultimate tensile stress of 1346 MPa. This estimation indicates that the increase of twinning stress may contribute to the deactivation of deformation twinning in $(CrCoNi)_{93}Al_4Ti_2Nb$ alloy.

4.2. Evolution of deformation substructure and strain hardening mechanism

As shown in the previous section, dislocation slip dominates plastic deformation of $(CrCoNi)_{93}Al_4Ti_2Nb$. Deformation substructures continuously evolve with increasing strain, which is illustrated in Fig. 18 at different stages of strain hardening. As mentioned before, the strain hardening curve can be roughly divided into two stages. In stage A, the strain hardening rate monotonically decreases with increasing strain, which is typical for engineering alloys. In this stage, dislocation arrays nucleate from sources at grain boundaries and within grains under the external loading. Due to slip planarity, dislocations are localized within slip bands. In order to shear through LRO $L1_2$ domains, dislocations tend to be paired. Dislocation multipoles act as slip barriers for further dislocation slip within grain interiors. These multipoles are also building blocks for the formation of subgrain structures in Stage B.

The present results provide insights into the creation of these multipole structures under co-planar deformation conditions in Stage A. These insights have been enabled by the inspection of large areas of grains made possible using the STEM-DCI technique, which minimizes the rapidly changing contrast due to natural bending of thin foils that limit effective fields of view in CTEM-DCI. The bright field STEM image in Fig. 19a shows another example of multipoles after deformation up to 0.6% plastic strain. An inset image in Fig. 19a presents an enlarged view of the step like structures of the multipole, revealing that the multipole was formed through the slip of dislocations on two adjacent $(1\bar{1}1)$ planes. Weak beam dark field STEM image in Fig. 19b shows a multipole consisting of less densely packed dislocations. It reveals the multipole was formed through the slip of dislocations with opposite signs as indicated by the contrast of dislocation 1 and dislocation 2 in the two

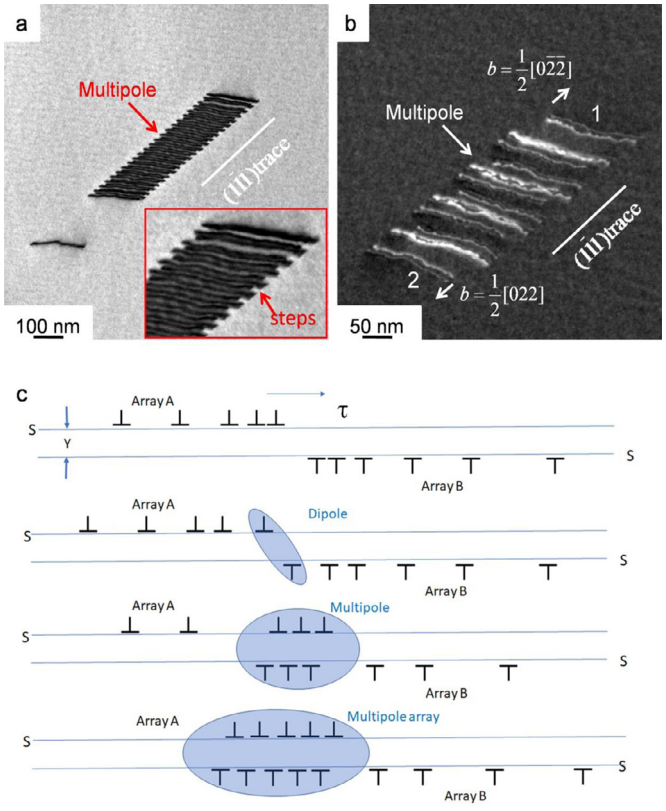

Fig. 19. (a) [100] Zone axis bright field STEM image with an inset image showing the step structure of a multipole; (b) weak beam dark field STEM image of a multipole consisting of less densely packed dislocations; and (c) conceptual explanation for the operation of two opposing, co-planar dislocation arrays and the sequential steps in formation of extended multipole structures.

arrays in the figure. Presented in Fig. 19c is a conceptual model for the development of the multipoles that are characteristic of the observed substructures, such as those seen in Figs. 11a, c and Fig. 19a. The multipoles sometime appear at the "tips" of isolated arrays. The pairing of dislocations at the tips of the arrays is ignored in the present discussion. It is hypothesized that these structures occur as a result of the interaction of opposite-sign dislocation arrays on parallel {111} planes that are within a critical offset distance (Y) such that they cannot bypass one another. An example of bypass is believed to be seen in Fig. 13. If Y is sufficiently small, then the stress fields of the leading dislocations in the two arrays interact strongly such that they are mutually "trapped" [76,77]. The net Burgers vector of this first dipole is zero, and thus it is favorable to form from a strain energy standpoint. Additional forward movement of dislocations in the two opposing arrays can be accommodated by breaking the first dipole, and creating a new set of two dipoles, as shown in step b in Fig. 19c. Not only does this further reduce the elastic strain energy, but it also enables the two arrays to do work in response to the applied shear stress. Repetition of this energetically favorable process will consume the dislocations in both arrays and create the extended multipole configurations observed experimentally and illustrated in step c in Fig. 19c. If the number of dislocations generated in the two arrays is not the same, then the excess dislocations in the array with the larger total number of dislocations (e.g. Array B in step d in Fig. 19c will remain with the multipole at the "tip" of the array. Note that the multipoles appear at the "tips" of isolated arrays. Dislocation simulations by Olfe and Neuhauser [82] showed that these "asymmetric" multipoles occur when a significant friction stress, which decreases as a function of shearing, is present. Since the multipoles have zero net Burgers vector, they do not create a long-range stress field. However, the multipoles do create "sinks" that effectively trap mobile dislocations [75,76]. While the source generating Array A in Fig. 19c could continue to operate, each dislocation produced will eventually become trapped by the multipole. The source producing Array B will be inhibited due to the back stress from the dislocations remaining in Array B. Nonetheless, previous analysis has indicated that work hardening due to multipoles is limited [77,83].

In stage B of strain hardening, dislocations on different slip systems operate extensively, resulting in the interaction of slip bands and further partitioning of grains. With increasing plastic deformation, the spacing between slip bands is continuously refined. Slip band refinement plays a crucial role in controlling strain hardening in the test alloy. The contribution to strength from different hardening mechanisms can be evaluated using the following equation [19,84]:

$$\sigma_{total} = \sigma_0 + \sigma_{ss} + \sigma_g + \sigma_{ordering} + \sigma_s \tag{3}$$

Where σ_0 is the strength contribution from Peierls-Nabarro lattice friction stress, σ_{SS} is the solid solution strengthening contribution, σ_g is the grain boundary strengthening, $\sigma_{ordering}$ is the contribution from both short range ordering and long range ordering, and σ_s is the contribution from dynamic grain refinement due to slip bands. Among those five strengthening contributions, the first three contributions (σ_0, σ_{ss}, and σ_g) can be regarded as independent of strain, while the last two continuously evolve with increasing plastic deformation.

The increase of strength due to the existence of LRO $L1_2$ domains can be evaluated using the following equation [70]:

$$\sigma_{ordering} = M\frac{\gamma_{APB}}{2b}\left(\sqrt{\frac{\gamma_{APB}d_s}{2T_L}}\frac{d_s}{L_s} - \frac{\pi}{4}\left(\frac{d_s}{L}\right)^2\right) \tag{4}$$

Where M is Taylor factor, γ_{APB} is anti-phase boundary energy, b is the magnitude of Burgers vector, d_s is the average size of ordered domains assuming that they are spherical, L_s is the spacing between LRO domains, T_L is the dislocation line tension and L is the center-to-center spacing between LRO domains, which can be estimated using the following equation [85]

$$L = \sqrt{\frac{8}{3\pi f}}d_s \tag{5}$$

where f is the volume fraction of ordered domains.

L_s can be given as [70]

$$L_s = \sqrt{\frac{8}{3\pi f}}d_s - d_s \tag{6}$$

T_L can be estimated using the following equation [86]:

$$T_L = \left(\frac{Gb^2}{2}\right) \tag{7}$$

The volume fraction of LRO $L1_2$ domains was measured to be around 0.25 based on APT results. The average size of LRO $L1_2$ domains is about 3.2 nm by averaging the results measured using HAADF imaging, APT and the number of paired dislocations. The average Taylor factor of the test alloy is around 3.1. Although the LRO $L1_2$ domains have an interconnected morphology, here we assume that the LRO $L1_2$ domains present themselves to gliding dislocations as discrete regions to estimate their contribution to strengthening. For an increase of yield strength of about 70MPa as compared with CrCoNi base alloy and assuming this increase of strength is mainly due to the contribution of LRO domains, the γ_{APB} of LRO domains is estimated to be around 122 mJ/m^2 using Eq. (4), which is much smaller than the APB energy of fully ordered $L1_2$ γ' precipitates in nickel-base superalloys (around 200 mJ/m^2) [70] or the APB energy of $L1_2$ ordered precipitates in high entropy alloys (198mJ/m^2) [87,88]. This estimation further shows that the ordering process within LRO domains may only be partially completed. γ_{APB}, b, T_L and f can be treated as constants in Eq. (4) throughout deformation. Therefore, according to Eq. 4, the strengthening contribution due to LRO $L1_2$ domains decrease with the decrease of the average size of LRO $L1_2$ domains (d_s).

As shown in Fig. 17, after the shearing of LRO $L1_2$ domains due to the slip of a train of paired dislocations, the sizes of LRO domains are reduced, while the volume fraction of LRO domains remains unchanged. Thus, according to Eq. 4, the contribution of LRO $L1_2$ domains to strengthening will continuously decrease with increasing plastic strain as more and more ordering domains are sheared by planar dislocation slip.

The contribution from dynamic slip band refinement to hardening can be evaluated using [19]:

$$\sigma_s = K \cdot M \cdot \mu \cdot b/D \tag{8}$$

Here, K is a geometrical factor, M is the Taylor factor, μ is the shear modulus, b is the magnitude of the Burgers vector, and D is the average spacing between slip bands. From this equation, we can see that the strengthening contribution from slip band refinement (σ_s) will continue to increase with dynamic refinement of slip band spacing.

Fig. 20 shows the measured mean spacing between slip bands as a function of plastic strain. With increasing plastic deformation, the average slip band spacing continuously decreases, indicating the increasing role of slip band refinement in strain hardening as shown in Eq. (8). In stage B of strain hardening, the dynamic slip band refinement may dominate the strain hardening process. However, dynamic slip refinement has a detrimental effect on slip planarity. With continuous refinement of slip bands, LRO

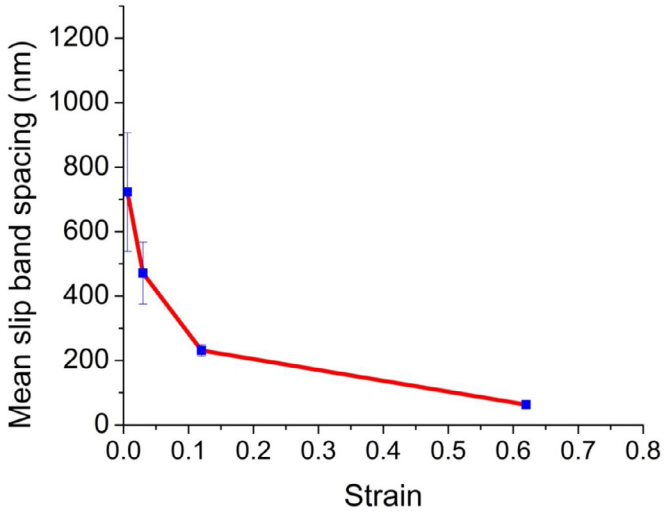

Fig. 20. The evolution of mean slip band spacing as a function of plastic strain.

$L1_2$ domains in the alloy will be increasingly refined or destroyed. HAADF STEM images of different magnifications in Fig. 21 show the microstructure of $(CrCoNi)_{93}Al_4Ti_2Nb$ after testing to rupture (62% strain). The inset FFT patterns in both STEM images show no superlattice reflections from LRO $L1_2$ domains, indicating the destruction of ordering domains due to plastic deformation. Therefore, the resistance that they pose to dislocation slip will gradually decrease, and thus the strictly planar dislocation slip character also gradually diminishes. Due to such effects, dislocation cross-slip and dynamic recovery become increasingly easier. Dislocation slip becomes more uniform rather than localized. Fig. 20 also shows that the slip band refinement rate at strain less than 12% is much higher than in the later stages of plastic deformation, indicating the weakening role of dynamic slip band refinement in the later stage of plastic deformation. Therefore, the contributions from both ordering and dynamic slip band refinement to strain hardening rates decrease in the late stage of plastic deformation.

Due to the existence of spatially-localized LRO $L1_2$ domains in $(CrCoNi)_{93}Al_4Ti_2Nb$ medium entropy alloy, dislocation slip has a strongly planar character. Work hardening is mainly controlled by dynamic refinement of slip bands. This deformation mechanism is different from that reported in equiatomic CrCoNi alloy [12,13] and Fe-Mn-Al-C alloys with high SFE. Microband-induced plasticity (MBIP) has been frequently observed in Fe-Mn-Al-C alloys with high SFE [17,18]. Current study shows that the deformation mechanisms in $(CrCoNi)_{93}Al_4Ti_2Nb$ medium entropy alloy are similar to those observed in lightweight steel with ordered secondary phases [19]. In both alloys, dislocation slip has strong planar character and work hardening is controlled by the dynamic refinement of slip bands.

As shown in Fig. 5, in the regime A of strain hardening rates, when strain is less than 4%, the strain hardening rate of $(CrCoNi)_{93}Al_4Ti_2Nb$ is higher than that of CrCoNi. In both alloys, planar dislocation slip is the main deformation substructures as observed in current study and previous work [13]. The higher strain hardening rate observed in $(CrCoNi)_{93}Al_4Ti_2Nb$ may be due to the existence of LRO $L1_2$ domains in $(CrCoNi)_{93}Al_4Ti_2Nb$. At around 4% strain, the strain hardening rates of both alloys are nearly equal. The deformation substructure in $(CrCoNi)_{93}Al_4Ti_2Nb$ is still dominated by planar dislocation slip and no extended stacking faults are observed, while in CrCoNi alloy, extended stacking faults have been frequently observed [13]. Those extended stacking faults act as precursors for the formation of deformation twinning and HCP phase. They may also contribute to strain hardening. In the regime B of strain hardening rate, the work hardening capability of two alloys are similar, as shown in Fig. 5 But the underlining mechanisms are different in two alloys as shown in current study and previous works [12,13]. Previous study shows that deformation twinning starts to nucleate in the CrCoNi alloy at around 9.7% and 12.9% strain at room temperature [12]. Deformation twinning becomes the dominant deformation mechanisms and FCC-HCP transformation further contribute to strain hardening in late stage of deformation in CrCoNi alloy [13], while in $(CrCoNi)_{93}Al_4Ti_2Nb$ alloy, as shown in current study, well-developed slip bands with fine spacing form at 12% strain and dynamic refinement within slip bands play a crucial role in controlling strain hardening. Although it is hard to decipher the respective contributions of each of these mechanisms to the total work hardening, the findings presented in this work suggest that LRO-dynamic slip band refinements may offer an alternative pathway as compared with TWIP-TRIP to improve strain hardening capability and ductility of engineering alloys. Further efforts are needed to better understand the role of such ordering structures on strengthening and strain hardening behavior of medium entropy alloys and high entropy alloys.

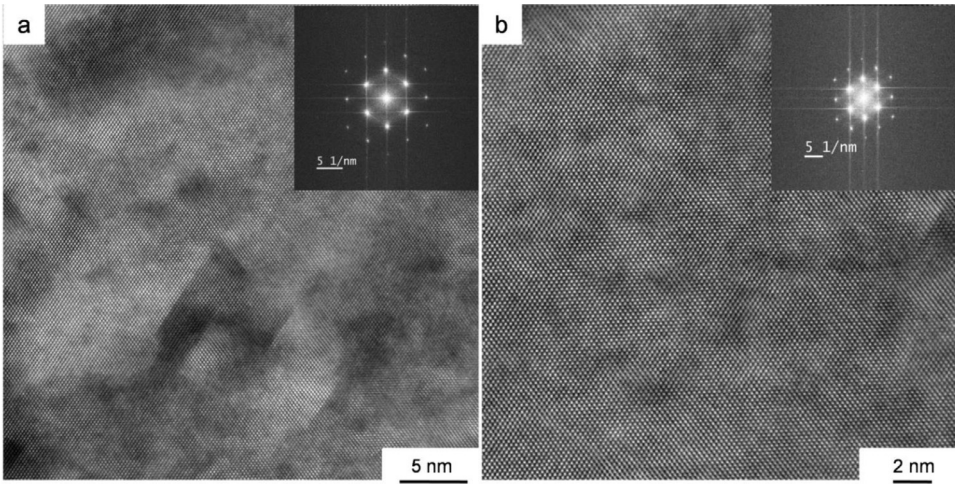

Fig. 21. HAADF-STEM images along [101] zone axis showing the microstructure of $(CrCoNi)_{93}Al_4Ti_2Nb$ after testing to rupture: (a) low magnification image; and (b) high magnification image.

5. Conclusions

In this work, the evolution of the deformation substructure in $(CrCoNi)_{93}Al_4Ti_2Nb$ was investigated using EBSD, ECCI and STEM based imaging techniques including weak beam dark field STEM. The observed microstructures and strain hardening behavior were correlated. Main findings are summarized as follows:

1. DF TEM imaging, HAADF-STEM imaging together with atom probe tomography study show the existence of spatially-localized LRO $L1_2$ domains in this alloy. The compositions of these LRO domains deviate from the equilibrium composition of γ' precipitates. The LRO domains may form through spinodal decomposition rather than nucleation and growth during the water quenching process used here.
2. Deformation in $(CrCoNi)_{93}Al_4Ti_2Nb$ occurs through the slip of narrowly dissociated $a/2\langle 110\rangle$ dislocations. No largely extended dissociated dislocations are observed. Dislocation slip has strongly planar character, which is mainly attributed to the relatively low stacking fault energy (~25 mJ/m^2) and the existence of LRO $L1_2$ domains. Due to such ordering domains, leading dislocations in slip bands tend to form paired dislocation structures. Based on the average number of paired dislocations within planar slip bands, the size of LRO domains was estimated to be 2.5 nm, which is close to the average size measured using HAADF STEM imaging (~3.1nm) and APT (~4nm). In the early stages of deformation, dislocation multipoles develop and act as obstacles to dislocation slip even under co-planar deformation conditions, and serve as building blocks for the formation of subgrain structures consisting of fine slip bands. Higher stacking fault energy (as compared with CrCoNi) and the existence of LRO $L1_2$ domains may contribute to the observed deactivation of deformation twinning in the $(CrCoNi)_{93}Al_4Ti_2Nb$ alloy
3. Dislocation slip dominates the deformation of $(CrCoNi)_{93}Al_4Ti_2Nb$. The spacing between slip bands decreases with increasing plastic deformation. Such dynamic slip band refinement plays a crucial role in controlling strain hardening behavior of the alloy. Due to slip planarity and dynamic slip band refinement, the role of the LRO $L1_2$ domains in strain hardening decreases with increasing plastic deformation. The planarity of dislocation slip gradually decreases due to reduction or destruction of spatially-localized LRO $L1_2$ domains through shearing by refined slip bands. Therefore, dislocation cross-slip and dynamic recovery become easier, which may be responsible for the decrease in strain hardening rates and more uniformly distributed dislocations observed at the late stage of plastic deformation.

Declaration of Competing Interest

The authors declare that they have no known competing financial interests or personal relationships that could have appeared to influence the work reported in this paper.

Acknowledgments

J. Miao, M. Ghazisaeidi, and M. J. Mills (EBSD, ECCI and TEM/STEM characterization) would like to thank the financial support from National Science Foundation under the contract No. # DMR-1905748. C.E. Slone (materials processing and mechanical testing) would like to thank the financial support from National Science Foundation under the contract No. # DMR-1905748 and support from the National Science Foundation Graduate Research Fellowship Program Grant No. DGE-1343012. E. P. George (materials synthesis) is supported by the U.S. Department of Energy, Office of Science, Basic Energy Sciences, Materials Sciences and Engineering Division. S. Dasari and R. Banerjee would like to acknowledge financial support from the US Air Force Office of Scientific Research under grant FA9550-17-1-0395. They would also like to acknowledge the Materials Research Facility (MRF) at the University of North Texas for use of microscopy and atom probe tomography facilities. The useful discussions regarding cluster analysis with Talukder Alam at Purdue University is acknowledged.

References

[1] B. Cantor, I.T.H. Chang, P. Knight, A.J.B. Vincent, Microstructural development in equiatomic multicomponent alloys, Mater. Sci. Eng. A. 375–377 (2004) 213–218.
[2] J.W. Yeh, S.K. Chen, S.J. Lin, J.Y. Gan, T.S. Chin, T.T. Shun, C.H. Tsau, S.Y. Chang, Nanostructured high-entropy alloys with multiple principal elements: novel alloy design concepts and outcomes, Adv. Eng. Mater. 6 (2004) 299–303.
[3] Y. Zhang, T.T. Zuo, Z. Tang, M.C. Gao, K.A. Dagmen, P.K. Liaw, Z.P. Lu, Microstructures and properties of high-entropy alloys, Prog. Mater. Sci. 61 (2014) 1–93.
[4] D.B. Miracle, O.N. Senkov, A critical review of high entropy alloys and related concepts, Acta Mater. 122 (2017) 448–511.
[5] E.P. George, D. Raabe, R.O. Ritchie, High-entropy alloys, Nat. Rev. Mater. 4 (2019) 515–534.
[6] E.P. George, W.A. Curtin, C.C. Tasan, High entropy alloys: a focused review of mechanical properties and deformation mechanisms, Acta Mater. 188 (2020) 435–474.
[7] B. Gludovatz, A. Hohenwarter, D. Catoor, E.H. Chang, E.P. George, R.O. Ritchie, A fracture-resistant high-entropy alloy forcryogenic applications, Science 345 (2014) 1153–1158.
[8] F. Otto, A. Dlouhý, C. Somsen, H. Bei, G. Eggeler, E.P. George, The influences of temperature and microstructure on the tensile properties of a CoCrFeMnNi high-entropy alloy, Acta Mater. 61 (2013) 5743–5755.
[9] G. Laplanche, A. Kostka, O.M. Horst, G. Eggeler, E.P. George, Microstructure evolution and critical stress for twinning in the CrMnFeCoNi high-entropy alloy, Acta Mater. 118 (2016) 152–163.
[10] Z. Wu, H. Bei, G.M. Pharr, E.P. George, Temperature dependence of the mechanical properties of equiatomic solid solution alloys with face-centered cubic crystal structures, Acta Mater. 81 (2014) 428–441.
[11] B. Gludovatz, A. Hohenwarter, K.V. Thurston, H. Bei, Z. Wu, E.P. George, R.O. Ritchie, Exceptional damage-tolerance of a medium-entropy alloy CrCoNi at cryogenic temperatures, Nat. Commun. 7 (2016) 10602.
[12] G. Laplanche, A. Kostka, C. Reinhart, J. Hunfeld, G. Eggeler, E.P. George, Reasons for the superior mechanical properties of medium-entropy CrCoNi compared to high-entropy CrMnFeCoNi, Acta Mater 128 (2017) 292–303.
[13] J. Miao, C.E. Slone, T.M. Smith, C. Niu, H. Bei, M. Ghazisaeidi, G.M. Pharr, M.J. Mills, The evolution of the deformation substructure in a Ni-Co-Cr equiatomic solid solution alloy, Acta Mater. 132 (2017) 35–48.
[14] Z. Li, K.G. Pradeep, Y. Deng, D. Raabe, C.C. Tasan, Metastable high-entropy dual-phase alloys overcome the strength-ductility trade-off, Nature 534 (2016) 227–230.
[15] Q. Lin, J. Liu, X. An, H. Wang, Y. Zhang, X. Liao, Cryogenic-deformation-induced phase transformation in an FeCoCrNi high-entropy alloy, Mater. Res. Lett. 6 (2018) 236–243.
[16] S. Chen, H. Oh, B. Gludovatz, S. Kim, E. Park, Z. Zhang, R.O. Ritchie, Q. Yu, Real–time observations of TRIP-induced ultrahigh strain hardening in a dual-phase CrMnFeCoNi high-entropy alloy, Nat. Commun. 11 (2020) 826.
[17] J.D. Yoo, K.-T. Park, Microband-induced plasticity in a high Mn-Al-C light steel, Mater. Sci. Eng. A. 496 (2008) 417–424.
[18] K.-T. Park, Tensile deformation of low-density Fe-Mn-Al-C austenitic steels at ambient temperature, Scr. Mater. 68 (2013) 375–379.
[19] E. Welsch, D. Ponge, S.M. Hafez Haghighat, S. Sandlöbes, P. Choi, M. Herbig, S. Zaefferer, D. Raabe, Strain hardening by dynamic slip band refinement in a high-Mn lightweight steel, Acta Mater. 116 (2016) 188–199.
[20] I. Gutierrez-Urrutia, D. Raabe, Multistage strain hardening through dislocation substructure and twinning in a high strength and ductile weight-reduced Fe–Mn–Al–C steel, Acta Mater 60 (2012) 5791–5802.
[21] D.T. Pierce, J.A. Jiménez, J. Bentley, D. Raabe, J.E. Wittig, The influence of stacking fault energy on the microstructural and strain hardening evolution of Fe–Mn–Al–Si steels during tensile deformation, Acta Mater. 100 (2015) 178–190.
[22] N.L. Okamoto, S. Fujimoto, Y. Kambara, M. Kawamura, Z.M. Chen, H. Matsunoshita, K. Tanaka, H. Inui, E.P. George, Size effect, critical resolved shear stress, stacking fault energy, and solid solution strengthening in the CrMnFeCoNi high-entropy alloy, Sci. Rep. 6 (2016) 35863.
[23] S.F. Liu, Y. Wu, H.T. Wang, J.Y. He, J.B. Liu, C.X. Chen, X.J. Liu, H. Wang, Z.P. Lu, Stacking fault energy of face-centered-cubic high entropy alloys, Intermetallics 93 (2018) 269–273.
[24] C. Niu, C.R. LaRosa, J. Miao, M.J. Mills, M. Ghazisaeidi, Magnetically-driven phase transformation strengthening in high entropy alloys, Nat. Commun. 9 (2018) 1363.

[25] T.M. Smith, M.S. Hooshmand, B.D. Esser, F. Otto, D.W. McComb, E.P. George, M. Ghazisaeidi, M.J. Mills, Atomic-scale characterization and modeling of 60° dislocations in a high-entropy alloy, Acta Mater. 110 (2016) 353–363.
[26] Q. Li, H. Sheng, E. Ma, Strengthening in multi-principal element alloys with local-chemical-order roughened dislocation pathways, Nat. Commun. 10 (2019) 3563.
[27] E. Ma, Unusual dislocation behavior in high-entropy alloys, Scr. Mater. 181 (2020) 127–133.
[28] V. Gerold, H.P. Karnthaler, On the origin of planar slip in f.c.c. alloys, Acta Metall. 37 (1989) 2177–2183.
[29] S.I. Hong, C. Laird, Mechanisms of slip mode modification in F.C.C. solid solutions, Acta Metall. Metall. 38 (1990) 1581–1594.
[30] K. Wolf, H.J. Gudladt, H.A. Calderon, G. Kostorz, Transition between planar and wavy slip in cyclically deformed short-range ordered alloys, Acta Metall. Mater. 42 (1994) 3759–3765.
[31] H. Neuhäuser, O.B Arkan, H.H. Potthoff, Dislocation multipoles and estimation of frictional stress in f.c.c. copper alloys, Mater. Sci. Eng. 81 (1986) 201–209.
[32] F.X. Zhang, S. Zhao, K. Jin, H. Xue, H.Bei G.Velisa, R. Huang, J.Y.P. Ko, D.C. Pagan, J.C. Neuefeind, W.J. Weber, Y. Zhang, Local structure and short-range order in a NiCoCr solid solution alloy, Phys. Rev. Lett. 118 (2017) 20551.
[33] J. Ding, Q. Yu, M. Asta, R.O. Ritchie, Tunable stacking fault energies by tailoring local chemical order in CrCoNi medium-entropy alloys, Proc. Natl. Acad. Sci. U. S. A. 115 (2018) 8919–8924.
[34] R. Zhang, S. Zhao, J. Ding, Y. Chong, T. Jia, C. Ophus, M. Asta, R.O. Ritchie, A.M. Minor, Short-range order and its impact on the CrCoNi medium-entropy alloy, Nature. 581 (2020) 283–287.
[35] Y.L. Zhao, T. Yang, Y. Tong, J. Wang, J.H. Luan, Z.B. Jiao, D. Chen, Y. Yang, A. Hu, C.T. Liu, J.-J. Kai, Heterogeneous precipitation behavior and stacking-fault mediated deformation in a CoCrNi-based medium-entropy alloy, Acta Mater. 138 (2017) 72–82.
[36] Z. Wu, W. Guo, K. Jin, J.D. Poplawsky, Y. Gao, H. Bei, Enhanced strength and ductility of a tungsten-doped CoCrNi medium-entropy alloy, J. Mater. Res. 33 (2018) 3301–3309.
[37] J. He, S.K. Makineni, W. Lu, Y. Shang, Z. Lu, Z. Li, B. Gault, On the formation of hierarchical microstructure in a Mo-doped NiCoCr medium-entropy alloy with enhanced strength-ductility synergy, Scr. Mater. 175 (2020) 1–6.
[38] I. Moravcik, H. Hadraba, L. Li, I. Dlouhy, D. Raabe, Z. Li, Yield strength increase of a CoCrNi medium entropy alloy by interstitial nitrogen doping at maintained ductility, Scr. Mater. 178 (2020) 391–397.
[39] D. Lee, M.P. Agustianingrum, N. Park, N. Tsuji, Synergistic effect by Al addition in improving mechanical performance of CoCrNi medium-entropy alloy, J. Alloys Compd. 800 (2019) 372–378.
[40] Y.Y. Shang, Y. Wu, J.Y. He, X.Y. Zhu, S.F. Liu, H.L. Huang, K. An, Y. Chen, S.H. Jiang, H. Wang, X.J. Liu, Z.P. Lu, Solving the strength-ductility tradeoff in the medium-entropy NiCoCr alloy via interstitial strengthening of carbon, Intermetallics 106 (2019) 77–87.
[41] Y. Ma, F. Yuan, M. Yang, P. Jiang, E. Ma, X. Wu, Dynamic shear deformation of a CrCoNi medium-entropy alloy with heterogeneous grain structures, Acta Mater 148 (2018) 407–418.
[42] M. Yang, D. Yan, F. Yuan, P. Jiang, E. Ma, X. Wu, Dynamically reinforced heterogeneous grain structure prolongs ductility in a medium-entropy alloy with gigapascal yield strength, Proc. Natl. Acad. Sci. U. S. A. 115 (2018) 7224–7229.
[43] C.E. Slone, J. Miao, E.P. George, M.J. Mills, Achieving ultra-high strength and ductility in equiatomicCrCoNi with partially recrystallized microstructures, Acta Mater. 165 (2019) 496–507.
[44] J.-P. Liu, J.-X. Chen, T.-W. Liu, C. Li, Y. Chen, L.-H. Dai, Superior strength-ductility CoCrNi medium-entropy alloy wire, Scr. Mater. 181 (2020) 19–24.
[45] H.W. Deng, Z.M. Xie, B.L. Zhao, Y.K. Wang, M.M. Wang, J.F. Yang, T. Zhang, Y. Xiong, X.P. Wang, Q.F. Fang, C.S. Liu, Tailoring mechanical properties of a CoCrNi medium-entropy alloy by controlling nanotwin-HCP lamellae and annealing twins, Mater. Sci. Eng. A. 744 (2019) 241–246.
[46] Y. Zhao, T. Yang, B. Han, J. Luan, D. Chen, W. Kai, C.T. Liu, J.J. Kai, Exceptional nanostructure stability and its origins in the CoCrNi-based precipitation-strengthened medium-entropy alloy, Mater. Res. Lett 7 (2019) 152–158.
[47] N. An, Y. Sun, Y. Wu, J. Tian, Z. Li, Q. Li, J. Chen, X. Hui, High temperature strengthening via nanoscale precipitation in wrought CoCrNi-based medium-entropy alloys, Mater. Sci. Eng. A 798 (2020) 140213.
[48] H. Peng, L. Hu, L. Li, W. Zhang, Ripening of L12 nanoparticles and their effects on mechanical properties of $Ni_{28}Co_{28}Fe_{21}Cr_{15}Al_4Ti_4$ high-entropy alloys, Mater. Sci. Eng. A 772 (2020) 138803.
[49] D. Chen, F. He, B. Han, Q. Wu, Y. Tang, Y. Zhao, Z. Wang, J. Wang, J.J. Kai, Synergistic effect of Ti and Al on L12-phase design in CoCrFeNi-based high entropy alloys, Intermetallics 110 (2019) 106476.
[50] B. Gwalani, V. Soni, D. Choudhuri, M. Lee, J.Y. Hwang, S.J. Nam, H. Ryu, S.H. Hong, R. Banerjee, Stability of ordered L12 and B2 precipitates in face centered cubic based high entropy alloys-$Al_{0.3}$CoFeCrNi and $Al_{0.3}$CuFeCrNi2, Scr. Mater 123 (2016) 130–134.
[51] T. Yang, Y. Zhao, W. Liu, J. Kai, C.T. Liu, L1 2-strengthened high-entropy alloys for advanced structural applications, J. Mater. Res 33 (2018) 2983–2997.
[52] B. Cao, T. Yang, W. Liu, C.T. Liu, Precipitation-hardened high-entropy alloys for high-temperature applications: a critical review, MRS Bulletin 44 (2019) 854–859.
[53] C.E. Slone, C.R. LaRosa, C.H. Zenk, E.P. George, M. Ghazisaeidi, M.J. Mills, Deactivating deformation twinning in medium-entropy CrCoNi with small additions of aluminum and titanium, Scr. Mater. 178 (2020) 295–300.
[54] J. Miao, S. Singh, J. Tessmer, M. Shih, M. Ghazisaeidi, M. DeGraef, M.J. Mills, Dislocation characterization using weak beam dark field STEM imaging, Microsc. Microanal. 24 (2018) 2202–2203.
[55] J.M. Hyde, E.A. Marquis, K.B. Wilford, T.J. Williams, A sensitivity analysis of the aximum separation method for the characterisation of solute clusters, Ultramicroscopy 111 (2011) 440–447.
[56] L.T. Stephenson, M.P. Moody, P.V. Liddicoat, S.P. Ringer, New techniques for the analysis of fine-scaled clustering phenomena within atom probe tomography (APT) data, Microsc. Microanal. 13 (2007) 448–463.
[57] U.F. Kocks, C.N. Tomé, H.-R. Wenk, Texture and Anisotropy: Preferred Orientations in Polycrystals and their Effect on Materials Properties, Cambridge University Press, 2000.
[58] W.O. Saxton, J. Frank, Motif detection in quantum noise-limited electron micrographs by cross-correlation, Ultramicroscopy 2 (1977) 219–227.
[59] J.V. Wood, P.F. Mills, J.K. Bingham, J.V. Bee, Structure and initial precipitation in a rapidly solidified nickel superalloy, Metall. Trans A. 10 (1979) 575–584.
[60] J.V. Wood, P.F. Mills, A.R. Wauch, J.V. Bee, Rapidly solidified nickel-based superalloys, J. Mater. Sci. 15 (1980) 2709–2719.
[61] H. Wendt, P. Haasen, Nucleation and growth of γ' precipitates in Ni-14 at% Al, Acta Metall. 31 (1983) 1649–1659.
[62] G.B. Viswanathan, R. Banerjee, A. Singh, S. Nag, J. Tiley, H.L. Fraser, Precipitation of ordered phases in metallic solid solutions: a synergistic clustering and ordering process, Scr. Mater. 65 (2011) 485–488.
[63] T. Rojhirunsakool, A.R.P. Singh, S. Nag, J.Y. Hwang, J. Tiley, R. Banerjee, Temporal evolution of non-equilibrium γ' precipitates in a rapidly quenched nickel base superalloy, Intermetallics 54 (2014) 218–224.
[64] X.P. Tan, D. Mangelinck, C. Perrin-Pellegrino, L. Rougier, C.-A. Gandin, A. Jacot, D. Ponsen, V. Jaquet, Spinodal decomposition mechanism of γ' precipitation in a single crystal Ni-based superalloy, Metall. Mater. Trans. A. 45 (2014) 4725–4730.
[65] R. Lawitzki, S. Hassan, L. Karge, J. Wagner, D. Wang, J. von, Kobylinski, C. Krempaszky, M. Hofmann, R. Gilles, G. Schmitz, Differentiation of γ'- and γ''- precipitates in Inconel 718 by a complementary study with small-angle neutron scattering and analytical microscopy, Acta Mater. 163 (2019) 28–39.
[66] C.E. Slone, S. Chakraborty, J. Miao, E.P. George, M.J. Mills, S.R. Niezgoda, Influence of deformation induced nanoscale twinning and FCC-HCP transformation on hardening and texture development in medium-entropy CrCoNi alloy, Acta Mater. 158 (2018) 38–52.
[67] E. Nembach, K. Suzuki, M. Ichihara, S. Takeuchi, In situ deformation of the γ' hardened superalloy Nimonic PE16 in high-voltage electron microscopes, Philos. Mag. A. 51 (1985) 607–618.
[68] R. Glas, M. Jouiad, P. Caron, N. Clement, H.O.K. Kirchner, Order and mechanical properties of the γ matrix of superalloys, Acta Mater. 44 (1996) 4917–4926.
[69] F. Pettinari, M. Prem, G. Krexner, P. Caron, A. Coujou, H.O.K. Kirchner, N. Clemént, Local order in industrial and model γ phases of superalloys, Acta mater. 49 (2001) 2549–2556.
[70] R.W. Kozar, A. Suzuki, W.W. Milligan, J.J. Schirra, M.F. Savage, T.M. Pollock, Strengthening mechanisms in polycrystalline multimodal nickel-base superalloys, Metall. Mater. Trans. A. 40 (2009) 1588–1603.
[71] Y. Yuan, Y.F. Gu, T. Osada, Z.H. Zhong, T. Yokokawa, H. Harada, Deformation mechanisms in a new disc superalloy at low and intermediate temperatures, Scr. Mater. 67 (2012) 137–140.
[72] G. Thomas, The effect of short-range order on stacking fault energy and dislocation arrangements in f.c.c. solid solutions, Acta Metall. 11 (1963) 1369–1371.
[73] C. Schlesier, E. Nembach, Strengthening of aluminum-lithium alloys by long-range ordered δ'- precipitates, Acta Metall. Mater. 43 (1995) 3983–3990.
[74] I. Baker, S. Guha, J.A. Horton, Transmission electron microscopy in situ straining of multiphase Ni-20at.%Al-30at.%Fe, Philos. Mag. A. 67 (1993) 663–674.
[75] T. Neeraj, M.J. Mills, Short-range order (SRO) and its effect on the primary creep behavior of a Ti–6wt.%Al alloy, Mater. Sci. Eng. A. 319–321 (2001) 415–419.
[76] N. Hansen, Low energy dislocation structures due to unidirectional deformation at low temperatures, Mater. Sci. Eng. 81 (1986) 141–161.
[77] H.S. Chen, J.J. Cilman, A.K. Head, Dislocation multipoles and their role in strain-hardening, J. Appl. Phys. 35 (1964) 2502–2514.
[78] D.J.H. Cockayne, I.L.F. Ray, M.J. Whelan, Investigations of dislocation strain fields using weak beams, Philos. Mag. 20 (1969) 1265–1270.
[79] B. Reppich, P. Schepp, G. Wehner, Some new aspects concerning particle hardening mechanisms in γ' precipitating nickel-base alloys—II, Exp., Acta Metall 30 (1982) 95–104.
[80] J. Miao, T.M. Pollock, J.W. Jones, Microstructural extremes and the transition from fatigue crack initiation to small crack growth in a polycrystalline nickel-base superalloy, Acta Mater. 60 (2012) 2840–2854.
[81] T.S. Byun, On the stress dependence of partial dislocation separation and deformation microstructure in austenitic stainless steels, Acta Mater. 51 (2003) 3063–3071.
[82] J. Olfe, H. Neuhäuser, Dislocation groups, multipoles, and friction stresses in α-CuZn alloys, Phys. Status Solidi. A 109 (1988) 149–160.
[83] P.M. Hazzledine, P.B. Hirsch, A critical examination of the long-range stress theory of work-hardening, Philos. Mag. 15 (1967) 121–159.
[84] U.F. Kocks, H. Mecking, Physics and phenomenology of strain hardening: the FCC case, Prog. Mater. Sci. 48 (2003) 171–273.
[85] A.J. Ardell, Precipitation hardening, Metall. Trans. A. 16 (1985) 2131–2165.
[86] B. Reppich, Some new aspects concerning particle hardening mechanisms in γ' precipitating Ni-base alloys—I. Theoretical concept, Acta Metall. 30 (1982) 87–94.

[87] T. Yang, Y.L. Zhao, Y. Tong, Z.B. Jiao, J. Wei, J.X. Cai, X.D. Han, D. Chen, A. Hu, J.J. Kai, K. Lu, Y. Liu, C.T. Liu, Multicomponent intermetallic nanoparticles and superb mechanical behaviors of complex alloys, Science 362 (2018) 933–937.

[88] M.S.K.K.Y. Nartu, T. Alam, S. Dasari, S.A. Mantri, S. Gorsse, H. Siller, N. Dahortre, R. Banerjee, Enhanced tensile yield strength in laser additively manufactured $Al_{0.3}$CoCrFeNi high entropy alloy, Materialia 9 (2020) 100522.